Spectrum oscillations from features in the potential of single-field inflation

I. Dalianis,[*] G. P. Kodaxis,[†] I. D. Stamou,[‡] N. Tetradis,[§] and A. Tsigkas-Kouvelis[‖]
Department of Physics, University of Athens, University Campus, Zographou 157 84, Greece

(Received 12 June 2021; accepted 19 October 2021; published 12 November 2021)

We study single-field inflationary models with steep steplike features in the potential that lead to the temporary violation of the slow-roll conditions during the evolution of the inflaton. These features enhance the power spectrum of the curvature perturbations by several orders of magnitude at certain scales and also produce prominent oscillatory patterns. We study analytically and numerically the inflationary dynamics. We describe quantitatively the size of the enhancement, as well as the profile of the oscillations, which are shaped by the number and position of the features in the potential. The induced tensor power spectrum inherits the distinctive oscillatory profile of the curvature spectrum and is potentially detectable by near-future space interferometers. The enhancement of the power spectrum by steplike features, though significant, may be insufficient to trigger the production of a sizable number of primordial black holes if radiation dominates the energy density of the early Universe. However, it can result in sufficient black hole production if the Universe is dominated by nonrelativistic matter. For the latter scenario, we find that deviations from the standard monochromatic profile of the mass spectrum of primordial black holes are possible because of the multiple-peak structure of the curvature power spectrum.

DOI: 10.1103/PhysRevD.104.103510

I. INTRODUCTION

A. Oscillations in the power spectrum

Inflationary models that predict deviations from scale invariance at small scales have been attracting a lot of attention in recent years. During the early evolution of the Universe, a strong enhancement of the spectrum of primordial scalar perturbations can trigger the gravitational collapse and the formation of primordial black holes (PBHs), which may survive until today in significant numbers in order to be detectable [1–4]. This possibility has been studied in great detail during the past years. (For reviews with extensive lists of references, see [5–8].) In addition, a potentially observable stochastic background of gravitational waves (GWs) is generated through the coupling of scalar and tensor modes at second order [9–18]. The induced tensors are suppressed by the small value of the scalar perturbations at the cosmic microwave background (CMB) scales [19], but may be sizable if the primordial density perturbations are enhanced at small scales. In this way, the relic GW stochastic background may provide a direct probe of the very early cosmic history. The detection prospects of induced GWs open a new window to probe the inflationary dynamics at small scales, for which CMB observables lack sensitivity.

A primordial scalar spectrum with a strong enhancement can be realized in various setups, such as through inflationary potentials that contain a near-inflection point [20–44], multifield inflation [45–57], modified gravity [58–63], curvaton models [64–67], sound speed modulation and parametric resonance [68–73]. It can also be realized when the inflationary potential features a steplike change [74–78], a framework that was revisited recently in [79]. It is very interesting that the enhancement profiles produced by these inflationary models may be distinguishable. Different inflationary realizations yield power spectra with a wide or narrow peak, oscillations or a multipeak structure.

In this work we focus on power spectra with oscillations around the peak. The oscillatory pattern is distinctive and possibly detectable, indicating a sharp feature in the inflationary dynamics. It can be caused by the reentry of k-modes in the horizon, a change in the sound speed [80], the backreaction of the entropy modes on the adiabatic modes in multifield inflation [55,81–83], or by a step in the inflaton potential [74–79,84–90]. The last example is the minimal realization of a sharp feature that involves single-field inflation dynamics and a canonical kinetic term. Motivated by the original proposal [74], where the effects of singular points in the inflationary potential were studied, we study here smooth variations of the basic setup, focusing on model-independent features. We compute analytically and numerically the evolution of

[*]idalianis@phys.uoa.gr
[†]gekontax@phys.uoa.gr
[‡]joanstam@phys.uoa.gr
[§]ntetrad@phys.uoa.gr
[‖]atsigkas@phys.uoa.gr

the curvature perturbations and find a strong enhancement of the scalar spectrum. In addition, we observe a burst of oscillations, generated solely by steplike changes in the inflaton potential.

As we show in the following section, a sharp drop in the potential of the inflaton field detunes the relative phase between the real and imaginary parts of the curvature perturbation, so that oscillations in the amplitude of the spectrum appear, while no reentry of modes takes place. The characteristic period of the oscillations depends on the position of the feature, while interference patterns are also apparent. We demonstrate that, even though the strong features in the underlying inflaton evolution may not be simple and the range of generated spectra extensive, an analytical understanding of their form is feasible. This is achieved by approximating the time-dependent inflaton background through a series of "pulses" that affect the evolution of the fluctuations. A similar approach has been followed in Refs. [91–93] in order to study inflation that is realized through a series of bursts of cosmic acceleration, separated by intervals of decelerated expansion. Our setup can be viewed as a reduced version of the so-called "rollercoaster cosmology" [92].

The amplitude of the peak of the spectrum of curvature perturbations $\mathcal{P}_R(k)$ is determined by the characteristics of the features in the inflaton potential, so that significant PBH production can be generated. It is exciting that the shape characteristics of the peak of the curvature spectrum can also be imprinted on the spectrum of induced GWs [55,81–83]. Specific realizations of this possibility involve nongeodesic motion during multifield inflation, or resonance effects. However, the link between strong features in the inflaton evolution and strong oscillations in the curvature and GW spectra is generic, as has been discussed in the above references.

In general, the $\mathcal{P}_R(k)$ characteristics are not clearly visible in the mass spectrum of the fractional PBH abundance $f_{\rm PBH}$, which appears predominantly monochromatic, mostly sensitive to the amplitude of the peak. Even though a universal behavior also appears in the GW spectrum [94], especially for smooth scalar spectra, the tensor perturbations are much more informative [17,95–97] and can display more clearly features originating in the scalar spectrum. In this way, the detection of stochastic GWs is a portal to the primordial spectrum of scalar perturbations at small scales, which can also be used to test the PBH dark matter scenario. Moreover, it can provide details of the possible strong features in the inflationary dynamics.

The induced GWs may be detected in the near future by the current and planned detectors. The LIGO collaboration has already produced upper limits in such stochastic backgrounds [98]. The searches will be further extended by a network of operating and designed gravitational wave detectors that will probe a vast range of different frequency bands. Pulsar time array GW experiments [99] have a sensitivity to the nano-Hz frequency band, space-based interferometers like LISA [100], Taiji [101], Tianqin [102], and Decigo [103,104] are mostly sensitive to milli-Hz and deci-Hz frequency bands, and the LIGO/Virgo and Einstein telescope [105] ground-based interferometers are sensitive to larger frequencies.

B. The steps in the inflaton potential

In the following section we shall discuss in detail the oscillatory patterns in the spectra of curvature perturbations and induced GWs that arise from steep steps in the inflaton potential. The steps connect regions in which the potential varies smoothly and the slow-roll conditions are satisfied. The basic pattern corresponds to the vacuum energy having one or more transition points at which it jumps from one constant value to another [79]. One can speculate that these points may correspond to values of the inflaton field at which certain modes, whose quantum fluctuations contribute to the vacuum energy, decouple very quickly. Decoupling effects become visible when the effective potential is regularized in a mass-sensitive scheme. Also, the dependence of the potential on an energy scale, or a coarse-graining length, can be analyzed through the Wilsonian approach to the renormalization group, see for example Refs. [106,107] for a particular implementation. The resulting renormalization-group equation for the potential can capture the decoupling behavior. However, our fundamental lack of understanding of the nature of vacuum energy or the cosmological constant does not permit a quantitative calculation of these effects.

Some intuition on this issue can be obtained by considering the role of underlying symmetries. A specific framework, which we shall use as the basis for the potentials that we shall consider, is provided by the models of α-attractors in supergravity [108,109]. A toy model that demonstrates the role of symmetries is described by the Lagrangian [110]

$$\mathcal{L}=\sqrt{-g}\left[\frac{1}{2}\partial_\mu\chi\partial^\mu\chi+\frac{1}{12}\chi^2R(g)-\frac{1}{2}\partial_\mu\phi\partial^\mu\phi-\frac{1}{12}\phi^2R(g)\right.$$
$$\left.-\frac{1}{36}F^2(\phi/\chi)(\chi^2-\phi^2)^2\right], \tag{1.1}$$

which is invariant under the conformal transformation

$$g_{\mu\nu}\to e^{-2\sigma(x)}g_{\mu\nu},\qquad \phi\to e^{\sigma(x)}\phi,\qquad \chi\to e^{\sigma(x)}\chi. \tag{1.2}$$

For constant $F(\phi/\chi)$, there is a global $SO(1,1)$ symmetry that keeps $\chi^2-\phi^2$ constant. The field χ does not have any physical degrees of freedom and can be eliminated through the gauge-fixing condition $\chi^2-\phi^2=6$. (All dimensionful quantities are expressed in units of $M_{\rm Pl}$.) We parametrize the fields as $\chi=\sqrt{6}\cosh(\varphi/\sqrt{6})$, $\phi=\sqrt{6}\sinh(\varphi/\sqrt{6})$ [110]. The Lagrangian becomes

$$\mathcal{L} = \sqrt{-g}\left[\frac{1}{2}R(g) - \frac{1}{2}\partial_\mu\varphi\partial^\mu\varphi - F^2\left(\tanh\frac{\varphi}{\sqrt{6}}\right)\right]. \quad (1.3)$$

A constant function $F(x)$, which preserves the $SO(1,1)$ symmetry, results in a cosmological constant in this formulation. The value of the cosmological constant is not constrained by the symmetry and is arbitrary.

We can introduce a minimal deformation of the symmetry by assuming that $F(x)$ takes two different values over two continuous ranges of x, with a rapid transition in between. A stronger deformation that has been used extensively in the literature assumes that $F(x)$ has a polynomial form. We shall employ a combination of the above choices by assuming that $F(x)$ has the schematic form

$$F(x) = x^n + \sum_i A_i\Theta(x - x_i), \quad (1.4)$$

allowing for more than one transition points. In order to avoid unphysical features in the evolution of the inflaton, each step function is replaced by a continuous function with a sharp transition at x_i. A more general framework is provided by the α-attractors [108–110]. The Lagrangian includes an additional free parameter α and takes the form

$$\mathcal{L} = \sqrt{-g}\left[\frac{1}{2}R(g) - \frac{1}{2}\partial_\mu\varphi\partial^\mu\varphi - F^2\left(\tanh\frac{\varphi}{\sqrt{6\alpha}}\right)\right]. \quad (1.5)$$

The potentials that result from our assumption for the function $F(x)$ with positive A_i are generalizations of the potential of the Starobinsky model [111], with the addition of one or more steep steps. Allowing for negative values of A_i makes it possible to include inflection points in the potential as well. As our analysis focuses on the phenomenological consequences of general features in the potential, we consider parameters A_i that can take values over the whole real axis. Another important feature of the potential in Eq. (1.5) is the sharpness of the transition between ranges of constant vacuum energy. This transition is modeled by a Θ-function in Eq. (1.4), but it is smooth in practice. Its steepness affects the oscillatory patterns appearing in the spectra. Because of our lack of understanding of the essence of the cosmological constant, we refrain from explicit model building, and treat the steepness as a free parameter. We only point out that the framework of α-attractors results in the dependence of the potential on $\tanh(\varphi/\sqrt{6\alpha})$, with α a free parameter. This allows, in principle, for potentials with transitions of arbitrary steepness.

C. Plan of the paper

The plan of the paper is as follows: In the next section we present an analytical discussion of the oscillatory patterns that can appear in the spectrum of curvature perturbations when the inflaton potential contains steplike features. We first establish our notation and identify the relevant parameters for the analysis of oscillations. We next use a simple toy model, neglecting the expansion of the background, in order to demonstrate how the detuning of the relative phase between the real and imaginary parts of the perturbation generates an oscillatory pattern in its amplitude. We then present an analytical study of the oscillatory form of the curvature power spectra that may result from strong features in the inflaton potential. This is possible if the effect on the fluctuations is modeled by a series of positive or negative pulses that correspond to the deviations from the slow-roll regime. In Sec. III we study explicit inflationary realizations with steplike features in the framework of α-attractors, paying particular attention to the consistency with the CMB constraints. For these inflationary models we examine the production of PBHs and their mass distribution, as well as the spectrum of the induced GWs. We elaborate on the relations and similarities between the patterns appearing in the curvature and tensor power spectra. Section IV contains our conclusions. All dimensionful quantities are given in units of $M_{\rm Pl}$ throughout the paper, unless the units are explicitly stated.

II. ANALYTICAL CALCULATION OF THE SPECTRUM OF CURVATURE PERTURBATIONS

A. General considerations

In this section we discuss an approximate analytical treatment of the spectrum of curvature perturbations in cases that the slow-roll approximation is strongly violated. We assume that the inflaton potential displays the standard plateau that can lead to an almost scale-invariant spectrum. In addition, it contains a strong feature within a finite range of field values, which can lead to the violation of the slow-roll conditions or even cause inflation to cease momentarily. In order to be as model independent as possible, we do not focus on specific potentials with these properties.

We consider the most general scalar metric perturbation around the Friedmann-Robertson-Walker (FRW) background [112],

$$ds^2 = a^2(\tau)\{(1+2\phi)d\tau^2 - 2B_{,i}dx^i d\tau - ((1-2\psi)\delta_{ij} + 2E_{,ij})dx^i dx^j\}, \quad (2.1)$$

with $B_{,i} = \partial_i B$, $E_{,ij} = \partial_i\partial_j E$. The inflaton field can be split into a background and a perturbation: $\varphi(\tau) + \delta\varphi(\tau, x)$. A gauge-invariant field perturbation can be defined as $v = a(\delta\varphi + (\varphi'/\mathcal{H})\psi)$, satisfying the Mukhanov-Sasaki equation [113,114],

$$v'' - \nabla^2 v - \frac{z''}{z}v = 0, \quad (2.2)$$

with $z = a\varphi'/\mathcal{H}$. The primes and the Hubble parameter refer to derivatives with respect to conformal time. The gauge-invariant comoving curvature perturbation $R = -v/z$ satisfies

$$R_k'' + 2\frac{z'}{z}R_k' + k^2 R_k = 0 \tag{2.3}$$

in Fourier space.

We shall use the number of e-foldings N as the independent variable for the evolution of the perturbations. The Hamilton-Jacobi slow-roll parameters are defined through the relations

$$H^2 = \frac{V(\varphi)}{3M_{\rm Pl}^2 - \frac{1}{2}\varphi_{,N}^2} \tag{2.4}$$

$$\varepsilon_H = -\frac{d\ln H}{dN} = \frac{\varphi_{,N}^2}{2M_{\rm Pl}^2} \tag{2.5}$$

$$\eta_H = \varepsilon_H - \frac{1}{2}\frac{d\ln\varepsilon_H}{dN} = \frac{\varphi_{,N}^2}{2M_{\rm Pl}^2} - \frac{\varphi_{,NN}}{\varphi_{,N}}, \tag{2.6}$$

where $H = e^{-N}\mathcal{H}$ is the Hubble parameter defined through cosmic time, and subscripts denote derivatives with respect to N. The parameter z is defined as $z = e^N\varphi_{,N}$. The effective equation of state for the background is $w = -1 + 2\varepsilon_H/3$. The equation for the curvature perturbation takes the form

$$R_{k,NN} + f(N)R_{k,N} + \frac{k^2}{e^{2N}H^2}R_k = 0, \tag{2.7}$$

with the quantity

$$f(N) = 3 + \frac{2\varphi_{,NN}}{\varphi_{,N}} - \frac{\varphi_{,N}^2}{2M_{\rm Pl}^2} = 3 + \varepsilon_H - 2\eta_H \tag{2.8}$$

playing a crucial role in determining the qualitative behavior of the solutions. In the slow-roll regime it acts as a generalized friction term. However, if η_H becomes positive and large it can lead to a dramatic enhancement of the perturbations.

In the approximation that the slow-roll parameters are neglected and H is assumed to remain constant, the solution of Eq. (2.7) can be expressed in terms of the Bessel functions $J_{\pm 3/2}$ as

$$R_k(N; C_p, C_m, 3) = Ae^{-\frac{3}{2}N}\left(C_p J_{3/2}\left(e^{-N}\frac{k}{H}\right) + C_m J_{-3/2}\left(e^{-N}\frac{k}{H}\right)\right), \tag{2.9}$$

where we take A to be real without loss of generality. For the values $C_p = 1$, $C_m = i$ the two Bessel functions combine into the Hankel function of the first kind $H_{3/2}^{(1)}$. The curvature perturbation is $R_k(N; 1, i, 3) \propto (e^{-ik\tau}/\sqrt{k})(1 - i/(k\tau))/a(\tau)$, where the conformal time is $H\tau = -e^{-N} = -1/a$. For $\tau \to -\infty$ this is the standard expression for the Bunch-Davies vacuum in the slow-roll regime, which is taken as the initial condition for the evolution of the fluctuations. For $\tau \to 0^-$ the curvature perturbation approaches a constant value $\propto k^{-3/2}$ as the mode with wave number k moves out of the horizon and freezes. The power spectrum of curvature perturbations $\Delta_R^2 = (k^3/2\pi^2)|R_k|^2$ is scale invariant. It is important to notice that the value of the curvature perturbation at late times, or $N \to \infty$, comes from the second term in Eq. (2.9), as the first one vanishes. In this sense, it is the absolute value of C_m that determines the power spectrum.

The above picture is modified when the function $f(N)$ of Eq. (2.8) deviates from a constant value equal to 3. For small values of ε_H, η_H the deviations from scale invariance can be computed analytically through the standard slow-roll analysis. However, our interest lies with strong modifications of ε_H, η_H that result in the enhancement of the spectrum by several orders of magnitude.

The typical forms of the effective-friction function $f(N)$ that we would like to analyze are depicted in Fig. 1. These examples result from an inflaton potential used in Ref. [79],

$$V(\varphi) = V_0\left(1 + \frac{1}{2}C(1 + \tanh(c\varphi)) + B\varphi\right), \tag{2.10}$$

for specific choices of its parameters. The function $f(N)$ remains close to 3, apart from a range of e-foldings in which it deviates strongly from this value. Similar features can be obtained with other types of potentials in single- or multifield inflation, such as potentials with inflection points, or multiple inflationary stages. The pattern can be repeated several times. When $f(N)$ becomes negative it induces a strong enhancement of the spectrum. The modifications to the spectrum appear for wave numbers of density perturbations deep in the nonlinear regime today.

In order to obtain an analytical solution, we model $f(N)$ through a sequence of square pulses, each with constant $f(N) = \kappa_i \neq 3$. At early and late times we assume that the inflaton is in a slow-roll regime, with negligible slow-roll parameters, so that $f(N) = 3$ and the curvature perturbation is given by Eq. (2.9). We approximate the Hubble parameter H as almost constant. This is a good approximation, as our focus is on modifications of the spectrum by several orders of magnitude. In comparison, the change in the Hubble parameter for an inflection point in the potential is less than 1%, while for a step in the potential it is of order 10%. We use an arbitrary normalization for the number of e-foldings by absorbing a factor of $\exp(N_0)$ in k, where N_0 corresponds to the actual number of e-foldings since the beginning of inflation until the moment in time that we denote by $N = 0$. In practice this means that the physical value of the wave number is $\exp(N_0)k$.

Our starting point is the solution (2.9), which defines the initial condition for $N \to -\infty$. For $C_p = 1$, $C_m = i$, this

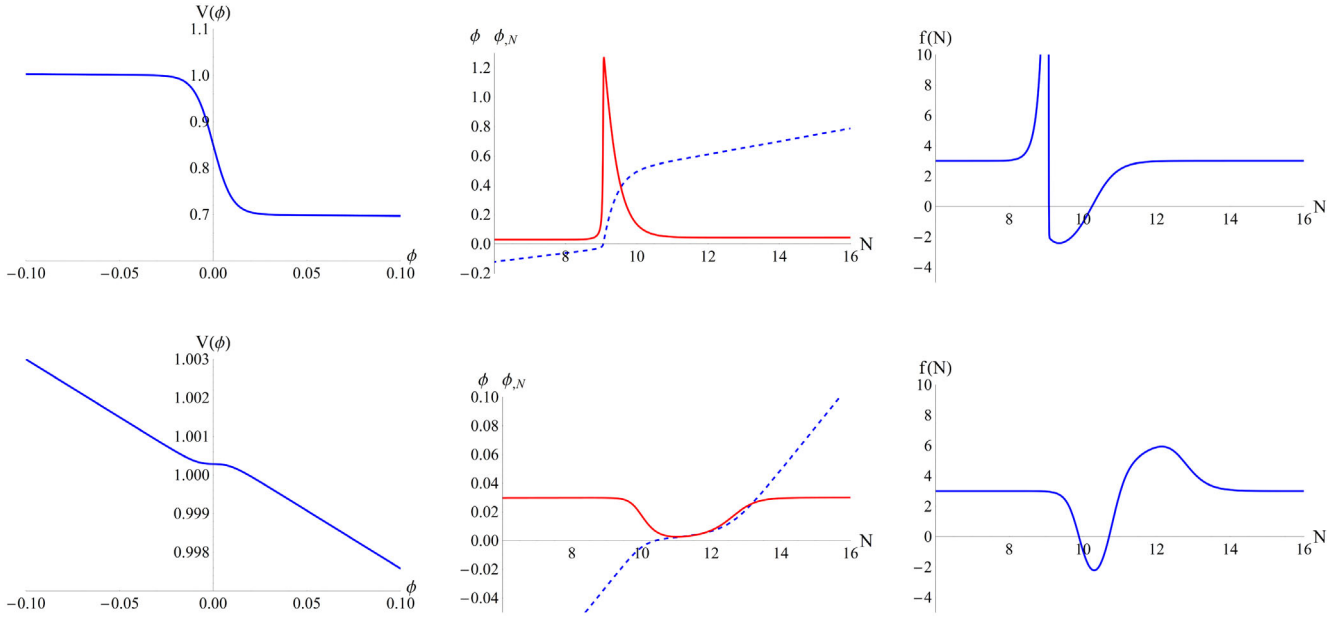

FIG. 1. The inflaton potential $V(\varphi)$ of Eq. (2.10), the evolution of the inflaton φ (dashed line) and its derivative $\varphi_{,N}$ (solid line), and the function $f(N)$ defined in Eq. (2.8), for two choices of the parameters of the potential: First row: $C = -0.3$, $c = 100$, $B = -0.03$; second row: $C = 0.00058$, $c = 100$, $B = -0.03$.

expression corresponds to the Bunch-Davies vacuum. We neglect slow-roll corrections and approximate the evolution through Eq. (2.9) until the value of N at which the first nontrivial pulse appears in $f(N)$. In the following subsection we analyze the modification of the curvature perturbation induced by this and the following pulses, until the system returns to a slow-roll regime. For $N \to \infty$ the solution becomes constant. We are interested in the relative increase of the asymptotic value of $|C_m|$ in comparison to the value $|C_m| = 1$ corresponding to a scale-invariant spectrum. In this sense, the value of the k-independent parameter A in Eq. (2.9) is not of interest to us. This parameter would determine the amplitude of the spectrum in the CMB region, and needs to be adjusted to a phenomenologically correct value.

An important point concerns the form of $f(N)$. Negative values of this function result only from η_H taking large positive values, as can be seen through Eqs. (2.5), (2.6), and (2.8). In general, large deviations from 3 can result from the term $2\varphi_{,NN}/\varphi_{,N}$ being the dominant one in Eq. (2.8). The integral of $f(N) - 3$ over N, from an early to a late slow-roll regime separated by nontrivial evolution, is

$$\begin{aligned}\int_{N_e}^{N_l} dN(f(N)-3) &= \int_{N_e}^{N_l} dN(\epsilon_H - 2\eta_H) \\ &= 2\log\frac{(\varphi_{,N})_l}{(\varphi_{,N})_e} + \log\frac{H_l}{H_e} \\ &= \log\frac{(dH/dN)_l}{(dH/dN)_e}, \end{aligned} \tag{2.11}$$

where we have used the definitions (2.5) and (2.6). This quantity is approximately zero for inflaton potentials with a strong feature localized within a region supporting slow-roll inflation and with similar values of dH/dN before and after the feature. In this work we neglect the slow-roll corrections and analyze only the very large enhancement resulting from such a strong feature, by imposing the constraint that positive and negative pulses have integrated areas that cancel.

B. Toy-model analysis

Several features that appear in the spectra that we study in the following sections can be understood in a much simpler context. We are interested in the effect of a pulse on the evolution of a mode with a free-wave initial condition. It is instructive to ignore the background expansion and consider the toy-model equation

$$R_{k,tt} + \kappa R_{k,t} + k^2 R_k = 0. \tag{2.12}$$

The solutions are oscillatory with an amplitude that gets suppressed or enhanced, depending on the sign of the friction parameter κ. It is straightforward to derive the solution for a friction term that vanishes at all times apart from the interval $0 < t < t_p$, by requiring the continuity of the solution and its first derivative at $t = 0$ and t_p.

For an early-time solution $R_k(t) = e^{-ikt}$, the evolution is depicted in Fig. 2. We observe the suppression of the amplitude for positive κ and the enhancement for negative κ. However, the most striking feature is the appearance of oscillations in the amplitude. Their origin lies in the

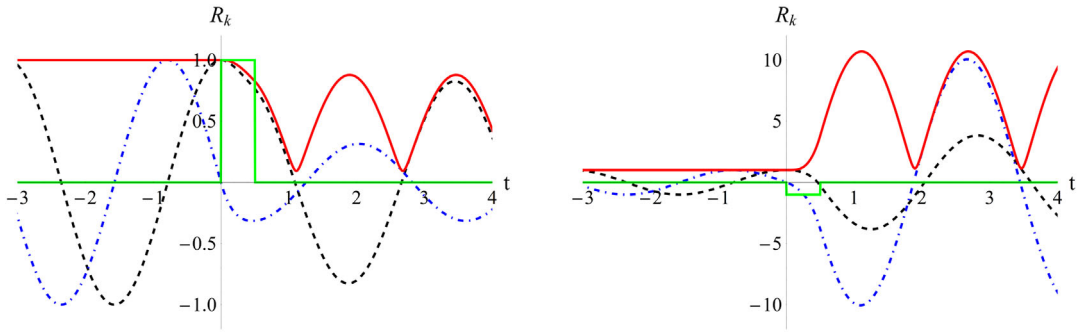

FIG. 2. The real part (dashed curve), imaginary part (dot-dashed curve) and amplitude (solid curve) of the solution of Eq. (2.12) with $k = 2$, for a pulse in the interval $0 \leq t \leq 0.5$. We also display the pulse, with a rescaled maximum $\kappa/5$. Left plot: $\kappa = 5$; right plot: $\kappa = -5$.

modification by the pulse of the relative phase between the real and imaginary parts. For sufficiently large $|\kappa|$ the relative phase in the late stage of the evolution almost vanishes (as in the plot), so that the amplitude approaches zero at certain instances. In the cosmological context, the oscillatory form of the evolution as a function of time can be transferred to the spectrum of perturbations. At late times, each mode k exits the horizon and eventually freezes. This can occur at any point of the oscillatory cycle, depending on the value of k. As a result, the asymptotic values of the perturbations depend strongly on the freezing time, and the spectrum displays oscillations as a function of k.

It is known that it is possible to obtain an oscillatory pattern in the spectrum if inflation stops for a certain time interval, so that modes that had exited the horizon reenter and start oscillating again until their next exit. Our toy example implies a more general pattern: Any feature during the evolution of the perturbations that detunes the relative phase between the real and imaginary parts of the solution results in an oscillatory spectrum, even if inflation is not halted.

Another interesting property of the late-time evolution is displayed in Fig. 3: The relative suppression of the amplitude of a mode for a given positive friction parameter κ is larger for higher wave number k. This is counterintuitive at first sight, as one would expect the last term of Eq. (2.12) to become more dominant for larger k and limit the suppression induced by the second term. However, the opposite happens. For small k, the strong friction tends to freeze the evolution during the pulse, so that the real and imaginary parts resume their oscillations after the pulse with amplitudes comparable to the initial ones. As a general rule of thumb, for a duration of the pulse of order 1, a strong suppression of the solution occurs for $k \gtrsim \kappa$.

C. Analytical expressions for pulses

We turn next to the analysis of Eq. (2.7). For constant $f(N) = \kappa$ the solution involves a linear combination of the Bessel functions $J_{\pm\kappa/2}$ and has the form

$$R_k(N; C_p, C_m, \kappa) = A e^{-\frac{1}{2}\kappa N}\left(C_p J_{\kappa/2}\left(e^{-N}\frac{k}{H}\right) + C_m J_{-\kappa/2}\left(e^{-N}\frac{k}{H}\right)\right). \tag{2.13}$$

Let us suppose that the coefficients of the solution C_{p_i}, C_{m_i} are known for a range of e-foldings for which κ takes a specific value κ_i. If this range is followed by a transition at

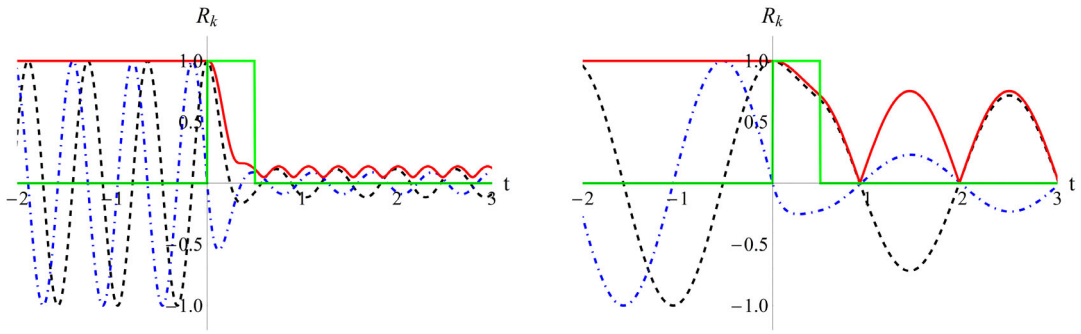

FIG. 3. The real part (dashed curve), imaginary part (dot-dashed curve) and amplitude (solid curve) of the solution of Eq. (2.12) for a pulse with $\kappa = 10$ in the interval $0 \leq t \leq 0.5$. We also display the pulse, with a rescaled maximum $\kappa/10$. Left plot: $k = 10$; right plot: $k = 3$, in arbitrary units.

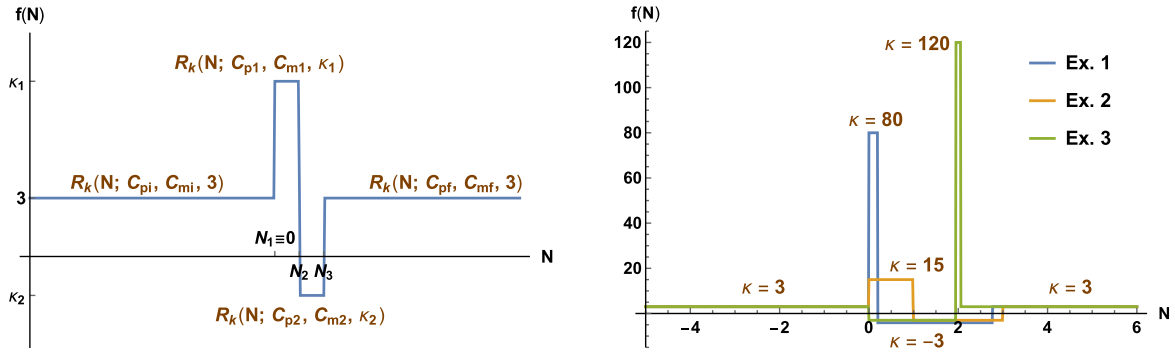

FIG. 4. An illustration of the approximate form of the function $f(N)$ that we assume for the analytical study. Left panel: a double-pulse model, with a positive-friction pulse followed by a negative-friction one. Right panel: the double-pulse form assumed in the three examples resulting in the spectra of Figs. 6–8.

$N = N_{fi}$ to a second range in which κ takes a different value κ_f, we would like to compute the corresponding values of the constants C_{p_f}, C_{m_f}, see Fig. 4. This can be achieved by requiring the continuity of the solution and its first derivative at $N = N_{fi}$. A similar analysis has been performed in Refs. [115,116], using conformal time as the independent variable. We aim here at providing a more transparent picture of the oscillatory patterns in the spectrum, by identifying the characteristic frequencies. Moreover, in the subsection we provide an analytical treatment that goes beyond the modeling of $f(N)$ through square pulses.

The new coefficients are given through the relation

$$\begin{pmatrix} C_{p_f} \\ C_{m_f} \end{pmatrix} = M(N_{fi}, \kappa_i, \kappa_f, k) \begin{pmatrix} C_{p_i} \\ C_{m_i} \end{pmatrix}, \tag{2.14}$$

where the matrix $M(N_{fi}, \kappa_i, \kappa_f, k)$ has components

$$\begin{aligned}
M_{11} &= C\left(J_{-\kappa_f/2}\left(e^{-N_{fi}}\frac{k}{H}\right)J_{-1+\kappa_i/2}\left(e^{-N_{fi}}\frac{k}{H}\right) + J_{1-\kappa_f/2}\left(e^{-N_{fi}}\frac{k}{H}\right)J_{\kappa_i/2}\left(e^{-N_{fi}}\frac{k}{H}\right)\right) \\
M_{12} &= C\left(-J_{-\kappa_f/2}\left(e^{-N_{fi}}\frac{k}{H}\right)J_{1-\kappa_i/2}\left(e^{-N_{fi}}\frac{k}{H}\right) + J_{1-\kappa_f/2}\left(e^{-N_{fi}}\frac{k}{H}\right)J_{-\kappa_i/2}\left(e^{-N_{fi}}\frac{k}{H}\right)\right) \\
M_{21} &= C\left(-J_{\kappa_f/2}\left(e^{-N_{fi}}\frac{k}{H}\right)J_{-1+\kappa_i/2}\left(e^{-N_{fi}}\frac{k}{H}\right) + J_{-1+\kappa_f/2}\left(e^{-N_{fi}}\frac{k}{H}\right)J_{\kappa_i/2}\left(e^{-N_{fi}}\frac{k}{H}\right)\right) \\
M_{22} &= C\left(J_{\kappa_f/2}\left(e^{-N_{fi}}\frac{k}{H}\right)J_{1-\kappa_i/2}\left(e^{-N_{fi}}\frac{k}{H}\right) + J_{-1+\kappa_f/2}\left(e^{-N_{fi}}\frac{k}{H}\right)J_{-\kappa_i/2}\left(e^{-N_{fi}}\frac{k}{H}\right)\right),
\end{aligned} \tag{2.15}$$

with

$$C = \frac{\pi}{2} e^{\frac{1}{2}N_{fi}(-2+\kappa_f-\kappa_i)} \frac{k}{H} \csc\left(\frac{\pi\kappa_f}{2}\right). \tag{2.16}$$

The matrix has the property $M(N_{fi}, \kappa_m, \kappa_f, k) \cdot M(N_{fi}, \kappa_i, \kappa_m, k) = M(N_{fi}, \kappa_i, \kappa_f, k)$. This implies that we can select the value $\kappa = 3$ as a reference point for all transitions between different values of κ.

The next step is to define a matrix corresponding to a pulse of height κ above the value corresponding to the scale-invariant case. This matrix can be defined as

$$M_{\rm pulse}(N_1, N_2, \kappa, k) = M(N_2, \kappa, 3, k) \cdot M(N_1, 3, \kappa, k). \tag{2.17}$$

As we explained earlier, the increase of the power spectrum relative to the scale invariant one is given by the value of $|C_m|^2$ after a mode of given k has evolved past the strong features in the background. A product of several $M_{\rm pulse}$ matrices can reproduce the final values of the coefficients (C_p, C_m) of the Bessel functions $J_{\pm 3/2}$ after the fluctuations have evolved from an initial configuration corresponding to $(C_p, C_m) = (1, i)$ through a period of strong features in the function $f(N)$. Clearly, it is possible to reconstruct any smooth function $f(N)$ in terms of short intervals of N during which the function takes constant values. Multiplying the corresponding $M_{\rm pulse}$ matrices would provide a solution to the problem of the evolution of perturbations. However, such an approach is not very efficient for a numerical solution. We are mainly interested in obtaining intuitive analytical expressions for forms of $f(N)$ such as those depicted in Figs. 1 and 4, for which a product of a small number of $M_{\rm pulse}$ matrices suffices.

Simple analytical expressions can be obtained in the limits of large and small k, using the corresponding expansions of the Bessel functions. For a large real argument we have

$$J_a(z)=\sqrt{\frac{2}{\pi z}}\left[\cos\left(z-\frac{a\pi}{2}-\frac{\pi}{4}\right)-\frac{4a^2-1}{8z}\sin\left(z-\frac{a\pi}{2}-\frac{\pi}{4}\right)+\mathcal{O}(z^{-2})\right]. \tag{2.18}$$

Using this expression we find for large k

$$M^{(\infty)}_{\rm pulse}(N_1,N_2,\kappa,k)=e^{-\frac{1}{2}(N_2-N_1)(\kappa-3)}\left\{\begin{pmatrix}1&0\\0&1\end{pmatrix}+\frac{1}{8}(\kappa-3)\frac{H}{k}\begin{pmatrix}S_{11}&S_{12}\\S_{21}&S_{22}\end{pmatrix}\right\}, \tag{2.19}$$

where

$$\begin{aligned}
S_{11}&=2e^{N_1}\sin\left(2e^{-N_1}\frac{k}{H}\right)-2e^{N_2}\sin\left(2e^{-N_2}\frac{k}{H}\right),\\
S_{12}&=-e^{N_1}\left(1+\kappa+2\cos\left(2e^{-N_1}\frac{k}{H}\right)\right)+e^{N_2}\left(1+\kappa+2\cos\left(2e^{-N_2}\frac{k}{H}\right)\right),\\
S_{21}&=e^{N_1}\left(1+\kappa-2\cos\left(2e^{-N_1}\frac{k}{H}\right)\right)-e^{N_2}\left(1+\kappa-2\cos\left(2e^{-N_2}\frac{k}{H}\right)\right),\\
S_{22}&=-2e^{N_1}\sin\left(2e^{-N_1}\frac{k}{H}\right)+2e^{N_2}\sin\left(2e^{-N_2}\frac{k}{H}\right).
\end{aligned} \tag{2.20}$$

Keeping the leading contribution, we find that the power spectrum is scale invariant at late times (or $N\to\infty$) for $k\to\infty$, but has a value multiplied by the factor

$$[\delta\Delta^{(\infty)}_R]^2=|C_m|^2=e^{-(N_2-N_1)(\kappa-3)}, \tag{2.21}$$

relative to its scale-invariant value for modes that have sufficiently small k, so that they exit the horizon and decouple very early with $C_m=i$, without being affected by the features in $f(N)$. The exponent in the above expression is simply the area of the pulse exceeding the value 3. For $\kappa>3$ the spectrum is suppressed, while for $\kappa<3$ it is enhanced. By breaking a general function $f(N)$ in infinitesimal pulses, it is easy to see that the enhancement is equal to the integral of $f(N)-3$ over N. The corrections subleading in H/k introduce oscillatory patterns in the spectrum. The characteristic periods can be deduced from Eq. (2.20). The spectrum is expected to vanish at intervals $\delta k/H=e^{N_1}\pi$ and $\delta k/H=e^{N_2}\pi$. Moreover, when $N_1\simeq N_2$ we expect interference patterns.

Analytical expressions for $k\to 0$ are more difficult to obtain because the (1,2)-component of the matrix $M_{\rm pulse}$ scales as $1/k$ in this limit. As a result, the effect of several pulses, which involves the product of several such matrices, is not described by a simple analytical expression. However, the components (2,1) and (2,2), which are relevant for the spectrum, are simpler. The (2,1)-component becomes nonzero only at order $(k/H)^3$, while the (2,2)-component is equal to $1+\mathcal{O}((k/H)^2)$. So, up to order $(k/H)^2$, the (2,2)-component is sufficient for the calculation of the spectrum. We give the result for the sequence of two pulses:

$$\begin{aligned}
M^{(0)}_{\rm pulse}(N_1,N_2,N_3,\kappa_1,\kappa_2,k)|_{2,2}&\equiv[M(N_3,\kappa_2,3,k)\cdot M(N_2,\kappa_1,\kappa_2,k)\cdot M(N_1,3,\kappa_1,k)]_{2,2}\\
&=1+\frac{1}{6}\left(\frac{k}{H}\right)^2\times\left[\frac{\kappa_1-3}{\kappa_1(\kappa_1-2)}(-2(\kappa_1-3)e^{N_1(\kappa_1-2)-N_2\kappa_1}+3(\kappa_1-2)e^{-2N_1}-\kappa_1e^{-2N_2})\right.\\
&\quad-\frac{2(\kappa_1-3)(\kappa_2-3)}{\kappa_2(\kappa_1-2)}(e^{N_3\kappa_2}-e^{N_2\kappa_2})(e^{-2N_2-N_3\kappa_2}-e^{N_1(\kappa_1-2)-N_2\kappa_1-N_3\kappa_2})\\
&\quad\left.+\frac{\kappa_2-3}{\kappa_2(\kappa_2-2)}(-2(\kappa_2-3)e^{N_2(\kappa_2-2)-N_3\kappa_2}+3(\kappa_2-2)e^{-2N_2}-\kappa_2e^{-2N_3})\right].
\end{aligned} \tag{2.22}$$

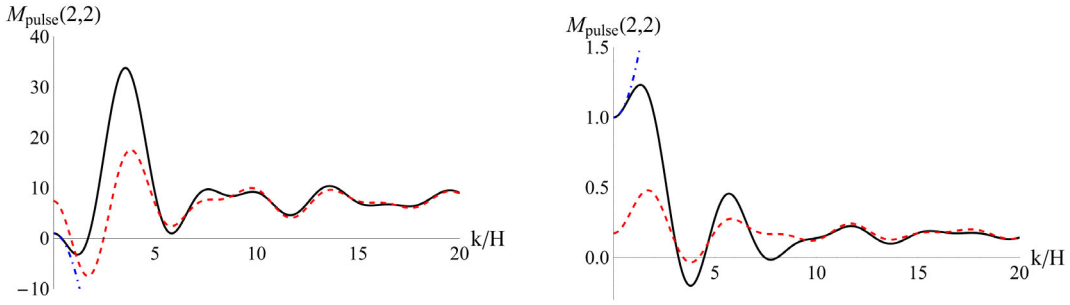

FIG. 5. The (2,2)-component of the matrix $M_{\rm pulse}$ defined in Eq. (2.17) (solid curve), along with the approximations for large k/H (dashed curve) and small k/H (dot-dashed curve). Left plot: $N_1 = 0$, $N_2 = 0.5$, $\kappa = -5$; right plot: $N_1 = 0$, $N_2 = 0.5$, $\kappa = 10$.

For $\kappa_2 = 3$ the second pulse is eliminated and only the first term in the bracket survives, while for $\kappa_1 = 3$ the first pulse is eliminated and the last term survives. For $\kappa_1, \kappa_2 \neq 3$ there is a mixing term, which indicates that the effects of the various pulses are not simply additive, even within this approximation.

The oscillatory behavior of the solutions can be observed in the components of the matrix $M_{\rm pulse}$ defined in Eq. (2.17). In Fig. 5 we depict the (2,2)-component of this matrix (solid lines) for $N_1 = 0$, $N_2 = 0.5$. This component gives the leading contribution to the power spectrum. The left plot corresponds to a negative-friction pulse with $\kappa = -5$ that causes the enhancement of the spectrum. The right plot is obtained for positive friction $\kappa = 10$ that leads to suppression. The asymptotic expansions of this component for large k/H (dashed curve), given by Eq. (2.19), and small k/H (dot-dashed curve), given by Eq. (2.22), are also plotted. Oscillatory behavior is observed, associated with interference patterns from two almost equal frequencies corresponding to $\delta k = e^{N_1}\pi$ and $\delta k = e^{N_2}\pi$. It is interesting that the oscillatory frequencies are correctly reproduced by the asymptotic expansion even for small k/H. Another feature that can be observed is the strong decrease of $M_{\rm pulse}$ for $k/H \gtrsim \kappa/2$ for positive κ, in agreement with the discussion at the end of the previous subsection.

D. The integral of $f(N)$

The form of $f(N)$ that we assume in our discussion should result from the time evolution of the parameters ε_H and η_H. We saw at the end of Sec. II A that the integral of this function over N is constrained by Eq. (2.11). In this subsection we discuss the type of field evolution, as given by the function $\varphi_{,N}$, which is consistent with our approximate treatment.

The Mukhanov-Sasaki equation (2.2) implies that the Wronskian of each Fourier mode of its solution

$$W[v_k] = -i(v_k v_k^{*\prime} - v_k^* v_k') \tag{2.23}$$

remains constant during the evolution. Here a prime denotes a derivative with respect to conformal time $\tau = -e^{-N}/H$. The solution of Eq. (2.2) plays the role of the mode function in the canonical quantization of the field v. For the Bunch-Davies vacuum, the initial condition at early times, when $k^2 \gg z''/z$, is chosen such that the mode function has the standard form in Minkowski spacetime. Selecting positive-energy solutions fixes the sign of the Wronskian to be positive, while the appropriate normalization results in $W[v_k] = 1$. This choice is automatically preserved at later times if v_k is a solution of Eq. (2.2). This can be seen by multiplying Eq. (2.2) by v_k^* and subtracting the conjugate of the same equation multiplied by v_k.

We have based our analysis on the curvature perturbation R_k, related to v_k through $R_k = -v_k/z$, with $z = e^N \varphi_{,N}$. The consistency of our approximation of describing $f(N)$ through a sequence of pulses implies a specific form of $\varphi_{,N}$ during the evolution through the strong features in the potential. We can deduce this form by considering the Wronskian of R_k:

$$W[R_k] = -i(R_k R_k^{*\prime} - R_k^* R_k') = \frac{W[v_k]}{z^2} = \frac{1}{z^2}. \tag{2.24}$$

The solution (2.13) gives

$$W[R_k] \propto i(C_p C_m^* - C_m C_p^*)\exp((1-\kappa)N). \tag{2.25}$$

Consistency with Eq. (2.24) requires that $\varphi_{,N} \propto \exp((\kappa-3)N/2)$. The inflaton "velocity" must grow fast with N for $\kappa > 3$, and decay for $\kappa < 3$. This is the behavior observed in Fig. 1. We have already mentioned that any function $f(N)$ can be reconstructed as a sequence of very short pulses of variable height κ. For small N the change of $\varphi_{,N}$, starting from some initial value at $N = 0$, is linear in N with a slope proportional to κ. Thus, by breaking $f(N)$ into many pulses one can obtain the required evolution of $\varphi_{,N}$ as a function of N. In this sense our analysis is very general. For consistency, of course, the deduced evolution must result from an appropriate inflaton potential.

Our main aim is to obtain an intuitive understanding of the form of the spectrum by focusing on the gross properties of $f(N)$. Let us consider a feature in the evolution resulting from two successive pulses with heights κ_1 and κ_2,

between early and late slow-roll regimes with $\kappa = 3$. The solution after the feature is traversed is given by Eq. (2.9) with

$$\begin{pmatrix} C_p \\ C_m \end{pmatrix} = M(N_3, \kappa_2, 3, k) \cdot M(N_2, \kappa_1, \kappa_2, k) \cdot M(N_1, 3, \kappa_1, k) \begin{pmatrix} 1 \\ i \end{pmatrix}, \tag{2.26}$$

where the matrix M is given by Eq. (2.15). Before the pulse we have $i(C_p C_m^* - C_m C_p^*)/2 = 1$, while after the pulse one finds

$$\frac{i}{2}(C_p C_m^* - C_m C_p^*) = e^{-(n_2-n_1)(\kappa_1-3)-(n_3-n_2)(\kappa_2-3)}. \tag{2.27}$$

The exponent is exactly (minus) the integral of $f(N) - 3$. By comparing the Wronskian $W[R_k]$ at late and early times (before and after the pulse), it becomes clear the quantity (2.27) is equal to the ratio $(\varphi_{,N}^2)_e/(\varphi_{,N}^2)_l$, with both quantities being constant. In this way we reproduce the result of Eq. (2.11), under our assumption that $H_l/H_e \simeq 1$.

Let us summarize the basic points: According to our assumptions, the system is in a slow-roll regime during an early and a late period, with values of the Hubble parameter that we have approximated as equal. We can assume that the values of $\varphi_{,N}$ are also approximately equal during these periods. These assumptions isolate the effect of the strong feature in the intermediate part of the evolution from the properties in the slow-roll regimes. During the intermediate part the inflaton velocity $\varphi_{,N}$ changes fast, by growing or decaying depending on the sign of $f(N) - 3$, as observed in Fig. 1. The integral of $f(N) - 3$ over N must vanish for $\varphi_{,N}$ to have equal values at early and late times. For realistic situations one must take into account the breaking of scale invariance in the slow-roll regimes as well. However, these are included in the standard slow-roll analysis and are not of interest to us here.

Finally, it can be checked through the asymptotic form of the Bessel functions that for both $k \to 0$ and $k \to \infty$, and for a vanishing integral of $f(N) - 3$, we have $(C_p, C_m) = (1, i)$ at all times during the evolution. This indicates that the low- and high-k modes are not affected by the presence of the feature. As a result the scale-invariant form of the spectrum is modified only for a finite range of wave numbers k.

E. The form of the spectrum

In this subsection we consider three examples of spectra that display the features we discussed in the previous subsection. The range of possible spectra is large, as we do not focus on a particular underlying model, but simply consider various forms of the function $f(N)$ defined in Eq. (2.8). We assume that the integral of $f(N) - 3$ over N vanishes, so that the spectrum is scale invariant with the same amplitude for very low and very high wave numbers k. We focus only on the relative enhancement of the spectrum at intermediate scales as a result of the presence of strong features in the underlying inflaton evolution. As the absolute scale of the spectrum is not of interest for our discussion, we set $A = 1$ in Eq. (2.9). We discuss next three particular examples of the form of the friction function $f(N)$.

In our first example (Example 1) the spectrum results from a function $f(N)$ of the qualitative form depicted in the first line of Fig. 1 and displayed explicitly in Fig. 4. The feature consists of a positive-friction pulse with $\kappa_1 = 80$ in the interval between $N_1 = 0$ and $N_2 = 0.2$, followed by a negative-friction pulse with $\kappa_2 = -3$ in the interval between $N_2 = 0.2$ and $N_3 = 2.77$. The value of the spectrum for a given value of k/H is equal to $|C_m|^2$, where (C_p, C_m) is given by Eq. (2.26). The result is depicted by the middle curve of the top plot in Fig. 6, in the k-range $k/H = 10^{-2}$–10^3 that corresponds to $N \simeq -4.6$ up to 6.9. In the same figure we also display the spectra that would result from a single pulse. These are computed from the expression

$$\begin{pmatrix} C_p \\ C_m \end{pmatrix} = M(N_2, \kappa_1, 3, k) \cdot M(N_1, 3, \kappa_1, k) \begin{pmatrix} 1 \\ i \end{pmatrix}, \tag{2.28}$$

for the positive-friction pulse (lower curve in Fig. 6), and

$$\begin{pmatrix} C_p \\ C_m \end{pmatrix} = M(N_3, \kappa_2, 3, k) \cdot M(N_2, 3, \kappa_2, k) \begin{pmatrix} 1 \\ i \end{pmatrix}, \tag{2.29}$$

for the negative-friction pulse (upper curve in Fig. 6). As we discussed in the previous subsection, the fact that the integral of the function $f(N) - 3$ over N does not vanish for these cases means that the quantity $\varphi_{,N}^2$ changes across the pulse by a factor equal to the exponential of this integral. The two slow-roll regimes are quite distinct in this case and the effect of the pulse is not clear. We display the spectra because they provide intuition on the features appearing in the two-pulse spectrum, for which the integral of $f(N) - 3$ vanishes. Details for the latter are presented in the next two plots of Fig. 6, for two successive k/H ranges on a linear horizonal axis. Notice the huge difference in the scale of the vertical axis in the two plots.

Several features of the spectra are apparent in these plots:

1. The two-pulse spectrum has a first minimum at a value of k/H well approximated by the positive root of the polynomial of Eq. (2.22).
2. The subsequent strong increase of the spectrum results from the effect of the negative-friction pulse. The spectrum reaches a maximal value comparable to that of the negative-friction single-pulse spectrum. A rough estimate can be obtained from the asymptotic value of the single-pulse spectrum, which is $\exp((N_3 - N_2)(3 - \kappa_2)) = \mathcal{O}(10^7)$.

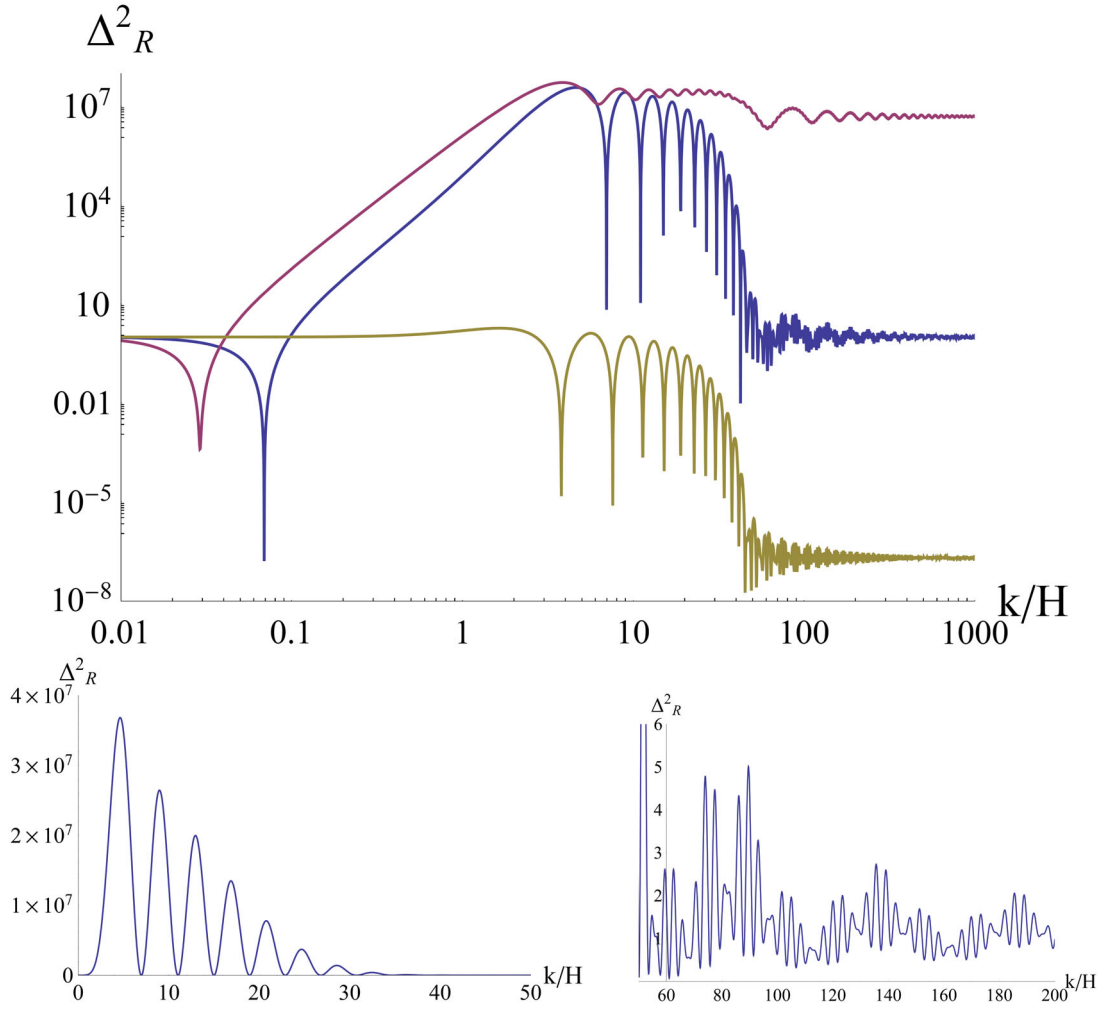

FIG. 6. Middle curve: spectrum resulting from a double pulse with $N_1 = 0$, $N_2 = 0.2$, $N_3 = 2.77$, $\kappa_1 = 80$, $\kappa_2 = -3$ (Example 1). Upper curve: spectrum resulting from a negative-friction single pulse with $\kappa_2 = -3$ between $N_2 = 0.2$, $N_3 = 2.77$. Lower curve: spectrum resulting from a positive-friction single pulse with $\kappa_1 = 80$ between $N_1 = 0$, $N_2 = 0.2$.

3. The envelope of the positive-friction single-pulse spectrum (lower curve) displays a sharp drop to almost zero at a characteristic value of k/H. As we discussed earlier, we expect that the positive friction will affect most strongly the high-k modes. A more quantitative estimate can be made by observing that the matrix M of Eq. (2.15) involves the Bessel functions $J_{\pm\kappa_1/2}$ and $J_{\mp1\pm\kappa_1/2}$. For large κ_1 these functions have a zero at a value of their argument roughly equal to $\kappa_1/2$. The relevant argument in our case is $e^{-\bar{N}}k/H$, with $\bar{N} \simeq (N_1 + N_2)/2$. Thus, we expect the spectrum to approach zero at $k/H \simeq e^{\bar{N}}\kappa_1/2 \simeq 44$, consistently with what is observed.
4. For $k/H \to \infty$, all three spectra become asymptotically constant, with values given by the exponential of the integral of $f(N) - 3$ over N. For the middle spectrum, we have fine-tuned this integral to zero, so that the spectrum returns to the value 1 to which we have normalized the spectrum for $k \to 0$.
5. Apart from the main features that we described above, which are consistent with the general expectations [117], the spectra display oscillations with characteristic scales. As we discussed in the previous subsection, the asymptotic expansions of Eq. (2.20) indicate that the spectrum should oscillate with periods $\delta k/H \simeq e^{N_1}\pi = 3.1$, $\delta k/H \simeq e^{N_2}\pi = 3.8$ and $\delta k/H \simeq e^{N_3}\pi = 50$. These characteristic modes, as well as interference patterns between them, are visible in the bottom plots of Fig. 6.

The most important conclusion that can be drawn from this example is that strong features in the background evolution can induce a spectrum of fluctuations which displays, apart from an enhancement by several orders of magnitude, strong oscillatory patterns. This is clearly visible in the bottom left plot of Fig. 6.

We turn next to our second example (Example 2). The oscillatory features in the spectrum are less pronounced for different forms of the pulses. Reducing the height of the

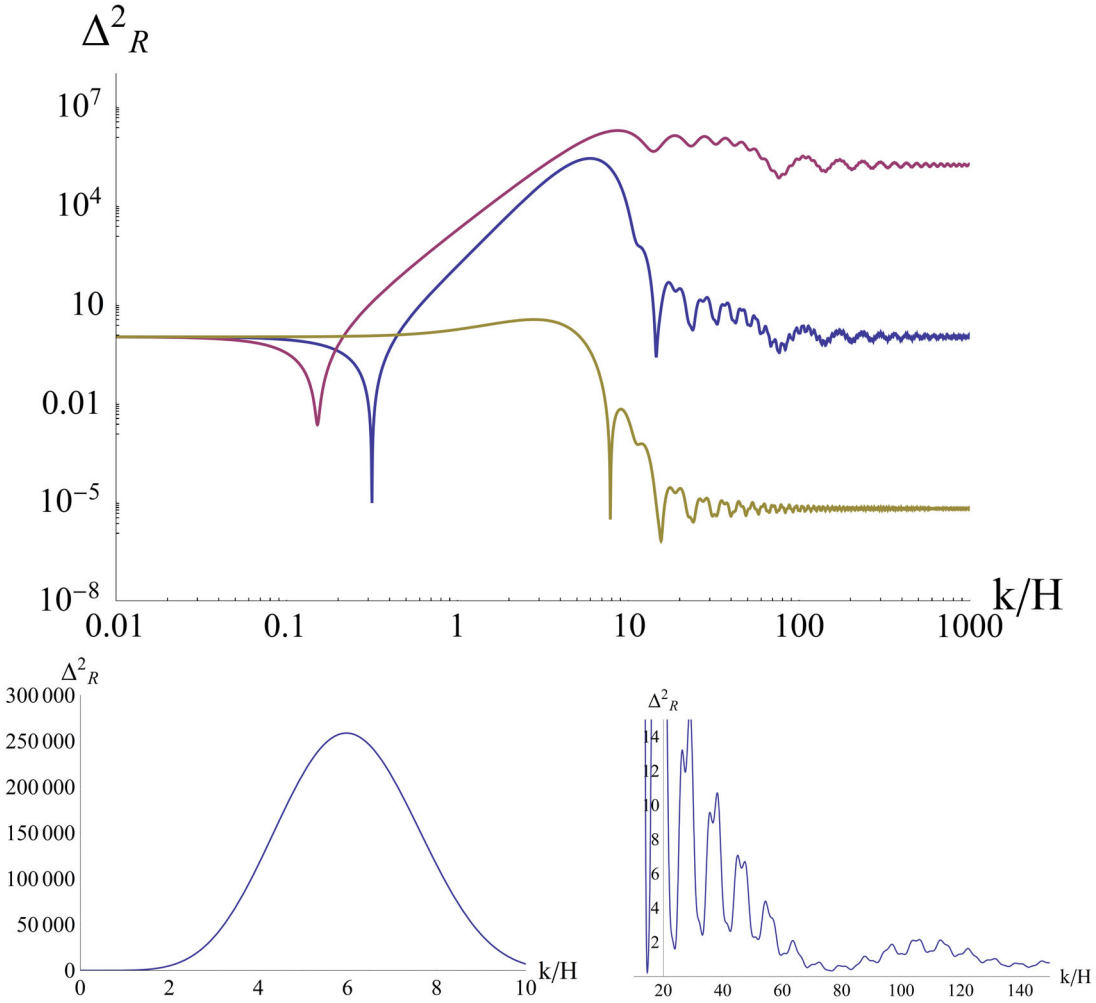

FIG. 7. Middle curve: spectrum resulting from a double pulse with $N_1 = 0$, $N_2 = 1$, $N_3 = 3$, $\kappa_1 = 15$, $\kappa_2 = -3$ (Example 2). Upper curve: spectrum resulting from a negative-friction single pulse with $\kappa_2 = -3$ between $N_2 = 1$, $N_3 = 3$. Lower curve: spectrum resulting from a positive-friction single pulse with $\kappa_1 = 15$ between $N_1 = 0$, $N_2 = 1$.

positive-friction pulse leads to a suppression of the spectrum at smaller values of k/H. As a result the oscillatory patterns may be confined within the high-k part of the spectrum, which does not get enhanced. This is visible in Fig. 7, where we plot the spectrum in the k-range, $k/H = 10^{-2}$–10^3 or from $N \simeq -4.6$ up to 6.9. The spectrum results from a positive-friction pulse with $\kappa_1 = 15$ in the interval between $N_1 = 0$ and $N_2 = 1$, followed by a negative-friction pulse with $\kappa_2 = -3$ in the interval between $N_2 = 1$ and $N_3 = 3$. The drop of the spectrum arising from only the positive-friction pulse is expected to appear at $k/H \simeq e^{\bar{N}}\kappa_1/2 \simeq 12$, where $\bar{N} \simeq (N_1 + N_2)/2$. Indeed, the small-$k$ region displays a large enhancement, but the oscillations appear only at large values of k/H, at which the spectrum is suppressed. The bottom left plot of Fig. 7 shows that the enhanced part of the spectrum is smooth in this case. The expected oscillatory modes with periods $\delta k/H \simeq e^{N_1}\pi = 3.1$, $\delta k/H \simeq e^{N_2}\pi = 8.5$ and $\delta k/H \simeq e^{N_3}\pi = 63$, as well as interference patterns between them, are visible in the bottom right plot of Fig. 7.

Our third example (Example 3) demonstrates that spectra with a different structure can result from different forms of the function $f(N)$. More specifically, the positive- and negative-friction pulses may occur in the reverse order compared to the one we assumed up until now. This is possible if the inflaton encounters a region of the potential with almost vanishing slope, as displayed in the second line of plots in Fig. 1. The reduction of the field velocity results in a period of positive values for the parameter η. When the inflaton moves beyond this region its velocity grows again, with η taking negative values. In Fig. 8 we plot the resulting spectra in the range $k/H = 10^{-2}$–10^3 ($N \simeq -4.6$ up to 6.9) considering an effective friction function $f(N)$ composed of a negative-friction pulse with $\kappa_1 = -3$ in the interval between $N_1 = 0$ and $N_2 = 1.95$, followed by a strong positive-friction pulse with $\kappa_2 = 120$ in the interval

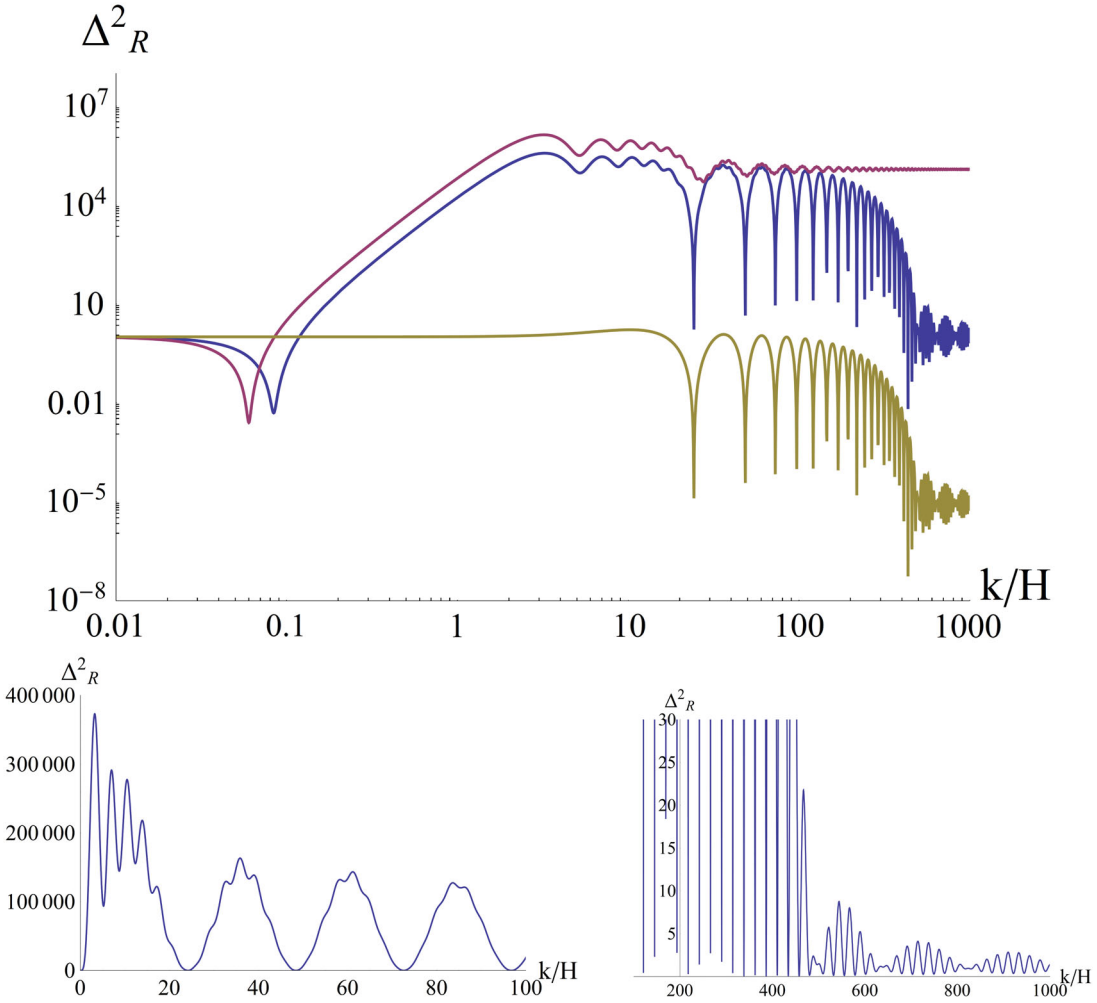

FIG. 8. Middle curve: spectrum resulting from a double pulse with $N_1 = 0$, $N_2 = 1.95$, $N_3 = 2.05$, $\kappa_1 = -3$, $\kappa_2 = 120$ (Example 3). Upper curve: spectrum resulting from a negative-friction single pulse with $N_1 = 0$, $N_2 = 1.95$, $\kappa_1 = -3$. Lower curve: spectrum resulting from a positive-friction single pulse with $\kappa_2 = 120$ between $N_2 = 1.95$, $N_3 = 2.05$.

between $N_2 = 1.95$ and $N_3 = 2.05$. The reduction of the spectrum is expected at a scale $k/H \simeq e^{\bar{N}}\kappa_2/2 \simeq 440$, where $\bar{N} \simeq (N_2 + N_3)/2$. The oscillatory patterns have characteristic periods $\delta k/H \simeq e^{N_1}\pi = 3.1$, $\delta k/H \simeq e^{N_2}\pi = 22.1$ and $\delta k/H \simeq e^{N_3}\pi = 24.4$. All these features, as well as strong interference patterns arising from the proximity of two characteristic periods, are visible in Fig. 8.

F. Analytical expressions for general $f(N)$

In this subsection we derive analytical expressions for the curvature spectrum resulting from an arbitrary friction function $f(N)$. We start by rewriting Eq. (2.7) as

$$R_{k,NN} + 3R_{k,N} + \frac{k^2}{e^{2N}H^2}R_k = (3 - f(N))R_{k,N}. \quad (2.30)$$

We would like to compute the Green's function $G(N)$ for the operator in the lhs. This function satisfies the equation

$$G_{k,NN}(N,n) + 3G_{k,N}(N,n) + \frac{k^2}{e^{2N}H^2}G_k(N,n) = \delta(N-n). \quad (2.31)$$

The solution of Eq. (2.30) is

$$R_k(N) = \bar{R}_k(N;1,i,3) + \int_{-\infty}^{\infty} G_k(N,n)(3-f(n))R_{k,n}(n)dn, \quad (2.32)$$

with

$$\bar{R}_k(N;1,i,3) = -\sqrt{\frac{2}{\pi}}\left(\frac{H}{k}\right)^{3/2}\left(i + e^{-N}\frac{k}{H}\right)\exp\left(ie^{-N}\frac{k}{H}\right) \quad (2.33)$$

the solution of the homogeneous equation, corresponding to $f(N) = 3$.

The evolution is classical, so we must use the retarded Green's function, which satisfies $G_{k>}(N, n) = 0$ for $n > N$. For $n < N$ the Green's function is

$$G_{k<}(N,n) = e^{-\frac{3}{2}N}\left(A(n)J_{3/2}\left(e^{-N}\frac{k}{H}\right) + B(n)J_{-3/2}\left(e^{-N}\frac{k}{H}\right)\right). \tag{2.34}$$

The total Green's function is continuous at $N = n$. Its first derivative has a discontinuity, obtained by integrating Eq. (2.31) around $N = n$. This gives $\partial G_{k<}(N,n)/\partial N|_{N=n} = 1$. Imposing these constraints results in

$$A(n) = -\sqrt{\frac{\pi}{2}}e^{3n}\left(\frac{k}{H}\right)^{-3/2}\left(\cos\left(e^{-n}\frac{k}{H}\right) + e^{-n}\frac{k}{H}\sin\left(e^{-n}\frac{k}{H}\right)\right) \tag{2.35}$$

$$B(n) = \sqrt{\frac{\pi}{2}}e^{3n}\left(\frac{k}{H}\right)^{-3/2}\left(e^{-n}\frac{k}{H}\cos\left(e^{-n}\frac{k}{H}\right) - \sin\left(e^{-n}\frac{k}{H}\right)\right). \tag{2.36}$$

Despite its simple form, it is difficult to find solutions of Eq. (2.32). However, the equation becomes simpler for $N \to \infty$, which is the limit of interest for the late-time spectrum. From Eq. (2.34) we obtain

$$G_{k<}(N,n) \to -\sqrt{\frac{2}{\pi}}\left(\frac{H}{k}\right)^{3/2}B(n) \tag{2.37}$$

in this limit. Equation (2.32) now becomes

$$R_k(\infty) = \bar{R}_k(\infty;1,i,3) - \sqrt{\frac{2}{\pi}}\left(\frac{H}{k}\right)^{3/2} \times \int_{-\infty}^{\infty}(3 - f(n))B(n)R_{k,n}(n)dn, \tag{2.38}$$

with

$$\bar{R}_k(\infty;1,i,3) = -i\sqrt{\frac{2}{\pi}}\left(\frac{H}{k}\right)^{3/2}. \tag{2.39}$$

Even though an analytical solution of this equation is not available, some conclusions about its form can be drawn when the function $f(N)$ displays strong features. The clearest example is a feature that can be approximated through a δ-function centered at N_1. The integration over n results in an expression that includes $\sin(e^{-N_1}k/H)$ and $\cos(e^{-N_1}k/H)$, producing oscillatory patterns. A similar conclusion can be reached if $f(N)$ involves sharp steplike features approximated through Θ-functions, as we discussed in the previous subsection. These patterns are expected to become less prominent when the features in $f(N)$ become smoother.

An approximate expression, which can be considered as the first step in an iterative solution of the above equation, can be obtained if we replace the full solution $R_k(n)$ in the integral with the solution for $f(n) = 3$, given by $\bar{R}_k(n,1,i,3)$. We have

$$\bar{R}_{k,n}(n,1,i,3) = \sqrt{\frac{2}{\pi}}\left(\frac{k}{H}\right)^{1/2}e^{-2n}\left(i\cos\left(e^{-n}\frac{k}{H}\right) - \sin\left(e^{-n}\frac{k}{H}\right)\right). \tag{2.40}$$

Combining the above expressions, we obtain

$$R_k(\infty) = \bar{R}_k(\infty;1,i,3)\left\{1 - i\frac{H}{k}\int_{-\infty}^{\infty}(3 - f(n))e^n\left[e^{-n}\frac{k}{H}\cos\left(e^{-n}\frac{k}{H}\right) - \sin\left(e^{-n}\frac{k}{H}\right)\right]\left[i\cos\left(e^{-n}\frac{k}{H}\right) - \sin\left(e^{-n}\frac{k}{H}\right)\right]dn\right\}. \tag{2.41}$$

This result is expected to be valid only for cases without a large enhancement of the spectrum. However, it is a compact expression that can be used in order to deduce the expected oscillatory patterns for a general form of $f(N)$.

In Fig. 9 we examine the validity of Eq. (2.41) for $f(N)$ with sharp and smooth features. In the left plot of the first line we depict the sharp and smoothed version (blue and red lines, respectively) of a friction function with moderate deviations from 3. In the right plot we depict the corresponding exact spectra (blue and red lines, respectively), as well as the ones computed through the approximate expression of Eq. (2.41) (black and orange lines, respectively). It is apparent that this expression captures with very good accuracy the complicated oscillatory patterns: the blue and black lines, as well as the red and orange lines, are in very good agreement. Small deviations from the exact solutions are observed when the amplitude becomes large. In the second line we repeat the calculation for a function $f(N)$ with very strong features that result in a large enhancement of the spectrum. The limitations of Eq. (2.41)

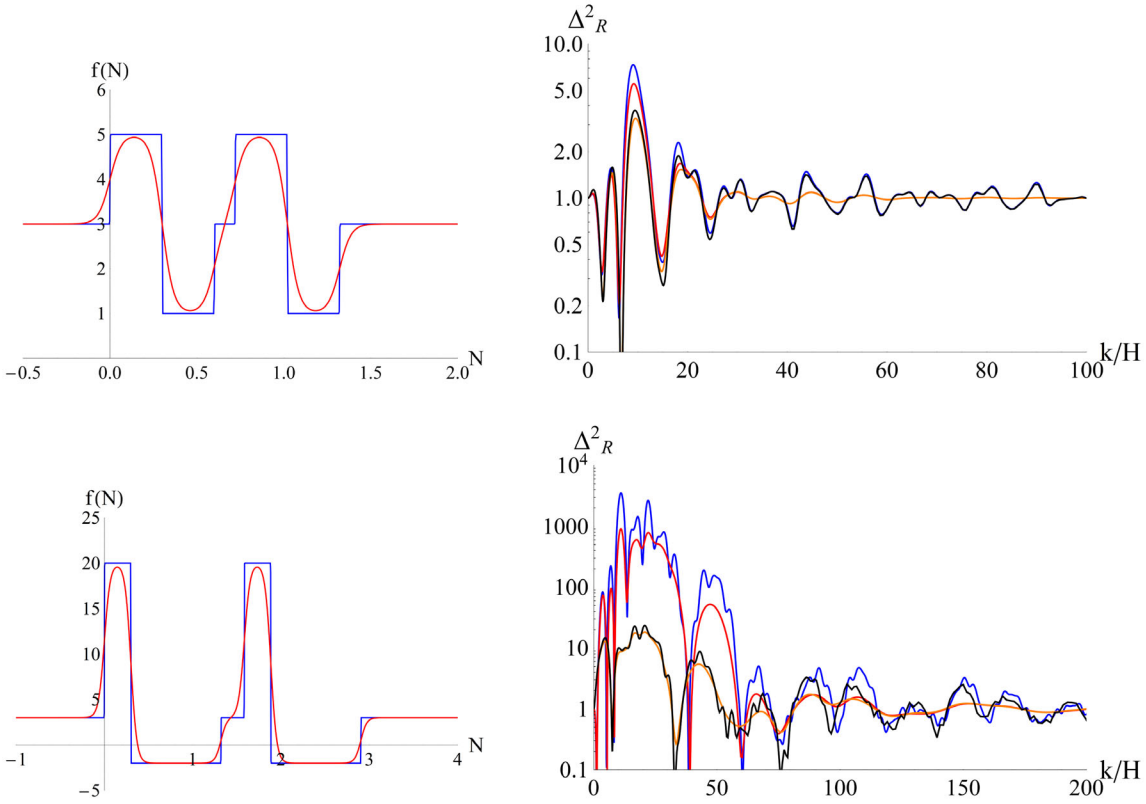

FIG. 9. Curvature power spectra for various forms of the friction function $f(N)$ (blue and red curves), compared to predictions by Eq. (2.41) (black and orange curves).

in capturing the magnitude of the enhancement become apparent. The agreement between black-blue lines and red-orange lines is good only for large values of k/H, for which the deviations from the scale-invariant spectrum are small [but still of O(1)]. Clearly, higher orders in the iterative solution of Eq. (2.38) are needed in order to capture the strong enhancement of the spectrum at small values of k/H.

Despite the limited range of validity of Eq. (2.41), it is interesting that the predicted oscillatory pattern appears in good agreement with the exact result in all cases. This indicates that the characteristic frequencies are determined by the convolution of the friction function $f(n)$ with the functions $\sin(e^{-n}k/H)$ and $\cos(e^{-n}k/H)$ in Eq. (2.38), even if $R_k(n)$ deviates strongly from the unperturbed solution $\bar{R}_k(n;1,i,3)$ of Eq. (2.33). In this respect, Eq. (2.41) provides the means for estimating the frequencies that appear in the power spectra for a general form of the friction function $f(N)$.

We also note that, as we saw in the previous subsection, the maximal enhancement of the spectrum for a single pulse can be estimated through the exponential of the integral of $3 - f(N)$ over the range that this function is positive. For patterns involving several pulses, the enhancement depends on their relative position [79]. However, the above estimate can be used as a (rough) guide for the maximal enhancement of the spectrum for the optimal position of the pulses.

III. PRIMORDIAL BLACK HOLES AND INDUCED GRAVITATIONAL WAVES

A. Specific inflationary models

Based on the discussion of Sec. I B that motivated the use of the framework of α-attractors, we assume the following form for the function F:

$$F(x) = F_0\left(x + \sum_{i=1}^{n} c_i \tanh(d(x - x_i))\right). \quad (3.1)$$

The corresponding inflationary potential for the field φ in the Einstein frame

$$V(\varphi) = F^2\left(\tanh\frac{\varphi}{\sqrt{6}}\right) \quad (3.2)$$

features n steplike transitions. (All dimensionful quantities are given in units of $M_{\rm Pl}$.) Such a potential can lead to an enhancement of the power spectrum of scalar perturbations [79] at particular scales, which can be sufficiently large to trigger PBH formation and induce detectable GWs. In addition, the shape of the scalar power spectrum around its

peak is characterized by an oscillatory pattern that can be inherited by the tensor power spectrum. We will discuss these notable phenomenological implications of potentials with steps in the next subsections.

The enhancement induced by a step has an upper bound corresponding roughly to a multiplicative factor $\exp(-\Delta N(\kappa-3))$, see Eq. (2.21). Here ΔN is the interval during which the value κ of the effective-friction term (2.8) is smaller than the value $\kappa=3$ that results in a scale-invariant spectrum. Negative values of κ are realized when the background inflaton "decelerates" on the lower plateau, after a sharp transition through a step in the potential. During this stage, which lasts a few e-foldings, we have $\varphi_{,NN}\simeq-3\varphi_{,N}$ and $\kappa\simeq-3$. As a result, a single step generally enhances the scalar power spectrum by roughly 2 or 3 orders of magnitude. However, it is possible that the potential includes several steplike features. In Fig. 10 we plot a set of specific examples of inflationary potentials with steps, described by Eq. (3.2). These potentials yield 50 to 60 e-foldings after the crossing of the CMB scale ($k=0.05$ Mpc^{-1}) and a spectral index value $n_s=0.969$, within the 68% C.L. range of Planck [118]. The parameters of these models are $c_i=7\times10^{-3}$. We consider from one ($n=1$) up to five steps ($n=5$) in Eq. (3.2), placed at $\varphi_1=5.7$, $\varphi_2=5.55$, $\varphi_3=5.4$, $\varphi_4=5.25$, $\varphi_5=5.1$, respectively. The value of F_0 is adjusted each time in order to be consistent with the measured amplitude of the spectrum at the CMB scale. For the initial value of the inflaton field we choose $\varphi_{\rm CMB}=6.33$, so as to obtain appropriate values for the spectral index n_s and the number of e-foldings N. The choice of the value of the parameter d is not crucial, as long as it is taken sufficiently large for the transition through the steps to occur quickly, but continuously. Typical values are of order 10^3–10^5.

We also examine the inflationary dynamics of models that feature both a step and a near-inflection point. The production of PBHs and induced GWs due to the presence of a near-inflection point in the framework of α-attractors has been studied in [34,37,97]. Such models result in a significant enhancement of the scalar power spectrum, while the presence of a steplike feature adds a prominent oscillatory pattern around the peak value. In Fig. 11 we plot an example of such a potential, within the α-attractor framework, with parameters $c_1=8.70\times10^{-2}$, $c_2=-2.77\times10^{-4}$. The step is placed at $\varphi_1=5.4$ and a shallow nearly inflection point exists at $\varphi_2=4.8$. The spectral index value for this model is $n_s=0.968$, within the 68% C.L. region of Planck [118]. The number of e-foldings after the crossing of the CMB scale is $N=51$ for an initial field value $\varphi_{\rm CMB}=6.17$. In Figs. 10 and 11 we also plot the function $f(N)$ that determines key characteristics of the scalar power spectrum, such as the amplitude and the oscillatory pattern, as discussed in Sec. II.

In the following subsections we examine the cosmological implications for PBH formation and GW production arising from the amplification of the scalar spectrum by the steplike features in the potential (3.2). Remarkably, models of this type yield striking predictions for the induced GWs that render them testable by the forthcoming GW detection experiments.

B. Primordial black holes

Inflationary potentials with steps enhance the amplitude of the primordial density perturbations at particular scales and might lead to gravitational collapse and PBH production. We review briefly observational bounds on the PBH abundance, relevant for our analysis.

In the largest part of the mass spectrum there are stringent upper bounds on $\Omega_{\rm PBH}/\Omega_{\rm DM}$ arising from observational constraints, see Fig. 12 for monochromatic PBH spectra. Light PBHs are constrained by the extragalactic gamma ray background (EGB); black holes of mass above 10^{17} g are subject to constraints from gravitational lensing of stars by Subaru (HSC), Ogle (O), EROS (E) and MACHO (M), microlensing of supernova (SN) and other experiments. The CMB anisotropies measured by Planck (PA) constrain the PBHs with masses above 10^{33} g. In the

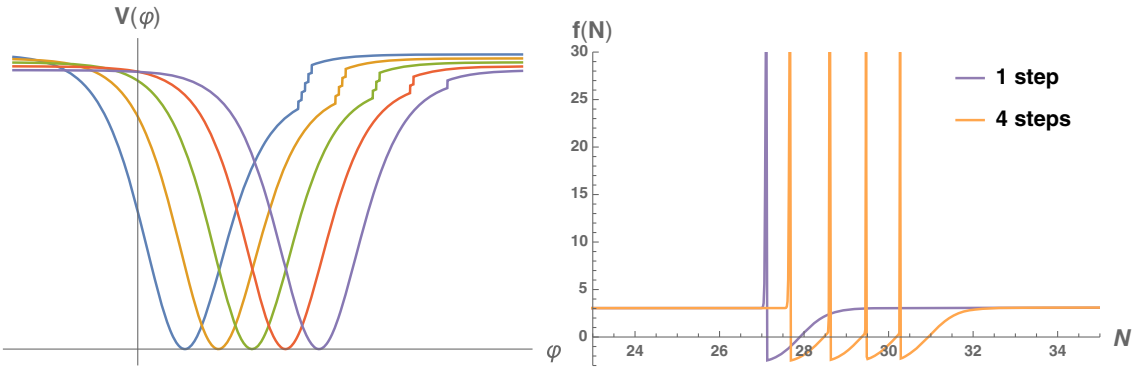

FIG. 10. Left panel: the inflationary potentials described by Eq. (3.2), arbitrary placed on the φ axis in order to make the steplike structure visible. Right panel: the function $f(N)$ of Eq. (2.8) in terms of the number of e-foldings for inflationary potentials with one and four steps.

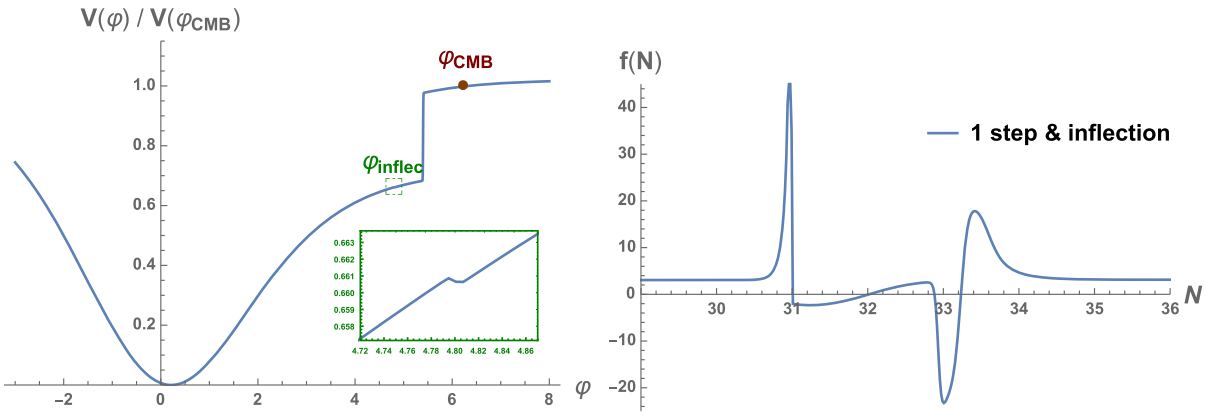

FIG. 11. Left panel: the inflationary potential with one step and an inflection point as a function of φ in Planck units. The model gives $n_s = 0.968$ for an initial field value $\phi_{\rm CMB} = 6.17\,M_{\rm Pl}$. The inflection point at $\phi_{\rm inflec} = 4.8\,M_{\rm Pl}$ is clearly visible through the magnification of the potential in the box. Right panel: the effective-friction function $f(N)$ during the part of the evolution in which it deviates from the standard value $f(N) \simeq 3$.

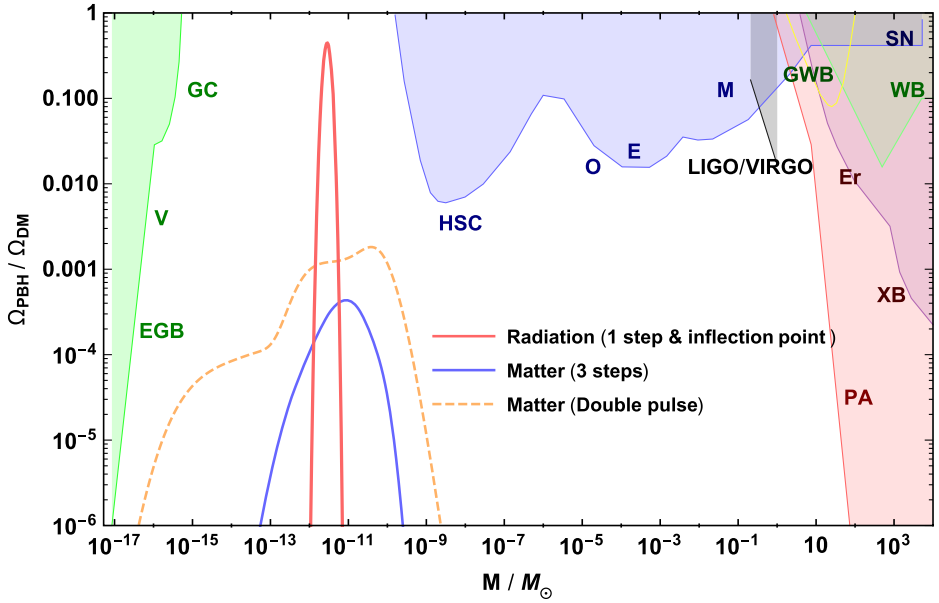

FIG. 12. The red curve depicts the abundance of PBHs produced by an inflationary model with a step and an inflection point during the RD era. The blue curve depicts the abundance of PBHs produced by an inflationary model with three steps during the MD era. The dashed curve is the PBH abundance produced during the MD era for the double-pulse model (termed Example 3) of Fig. 8, in which a negative-friction pulse is followed by a positive-friction pulse.

large-mass region there are also constraints from accretion limits in x-ray and radio observations and x-ray binaries (XB), and dynamical limits from disruption of wide binaries (WB) and survival of star clusters in Eridanus II (Er). Advanced LIGO/Virgo searches for compact binary systems with component masses in the range 0.2–1 $M_\odot$ find no GW events. For a detailed discussion and references on the PBH constraints we refer the reader to [119].

The maximal value of the PBH abundance can be achieved in the mass range $M_{\rm PBH} \sim 10^{-15}$–$10^{-10}\ M_\odot$. In this work we focus on this mass window that can be tested by near-future GW experiments, such as LISA. Nonetheless, the parameters of the same inflationary model with steplike features can be adjusted in order to generate PBHs in other mass windows, such as the $\mathcal{O}(10)$ solar mass window that is relevant for the LIGO/Virgo observed events.

The theoretical framework for the PBH formation that we shall follow next is based on the traditional Press-Schechter formalism [120]. Large density perturbations can create overdense regions that may collapse to form black holes after the horizon reentry. We examine separately the two most interesting cosmological scenarios for the very early Universe: the radiation (RD) and matter domination (MD) scenarios.

1. Radiation-dominated era

For a Gaussian distribution function of the primordial density perturbations and for spherically symmetric regions, the mass fraction of PBHs at formation is

$$\beta(M) = \int_{\delta_c} d\delta \frac{1}{\sqrt{2\pi\sigma^2(k)}} e^{-\frac{\delta^2}{2\sigma^2(k)}} \simeq \frac{1}{2}\mathrm{erfc}\left(\frac{\delta_c}{\sqrt{2}\sigma(k)}\right) \simeq \frac{1}{\sqrt{2\pi}}\frac{\sigma(k)}{\delta_c} e^{-\frac{\delta_c^2}{2\sigma^2(k)}}. \tag{3.3}$$

The parameter δ_c is the threshold density perturbation and $\mathrm{erfc}(x)$ is the complementary error function. For $\delta > \delta_c$ density perturbations overcome internal pressure and collapse. The β parameter can be regarded as the probability that the density contrast is larger than δ_c. The PBH abundance is exponentially sensitive to the threshold δ_c. Different values for δ_c are quoted in the literature, see e.g., [4,121–127], so that its precise value seems to be rather uncertain. In the comoving gauge, Ref. [125] finds $\delta_c = 0.41$ for $w = 1/3$. Numerical simulations demonstrate that there is no unique value for the threshold, because it depends on the density profile.

In the comoving gauge, assuming a nearly scale-invariant curvature power spectrum for a few e-folds around horizon crossing, the curvature perturbation R can be related to the density perturbation δ as $\delta(k,t) = 2(1+w)/(5+3w)(k/aH)^2 R(k,t)$. The variance of the density perturbations $\sigma(k)$, smoothed on a scale k in the radiation-dominated era, is given by [128]

$$\sigma^2(k) = \left(\frac{4}{9}\right)^2 \int \frac{dq}{q} W^2(qk^{-1})(qk^{-1})^4 \Delta_R^2(q), \tag{3.4}$$

where $\Delta_R^2(q)$ is the power spectrum of the curvature perturbations, usually calculated numerically. Here $W(z)$ represents the Fourier transform of the Gaussian window function. In order to estimate the mass spectrum of the PBHs, the horizon scale at the time of reentry of the perturbation mode k has to be related to the mass of formed PBHs. During the radiation era, the wave number scales as $k \propto g_*^{1/2} g_s^{-2/3} S^{2/3} a^{-1}$ and the Hubble horizon as $H \propto g_*^{1/2} g_s^{-2/3} S^{2/3} a^{-2}$, where S denotes the entropy, and g_*, g_s count the total number of the effectively massless degrees of freedom for the energy and entropy densities respectively. Assuming conservation of the entropy between the reentry moment and the epoch of radiation-matter equality, the relation between the PBH mass M and the comoving wave number k is given by

$$M(k) = \gamma\rho \frac{4\pi H(k)^{-3}}{3}\bigg|_{k=aH} \simeq 2.4\times 10^{-16}\, M_\odot \left(\frac{\gamma}{0.2}\right) \times \left(\frac{g_*(T)}{106.75}\right)^{-\frac{1}{6}} \left(\frac{k}{10^{14}\ \mathrm{Mpc}^{-1}}\right)^{-2}, \tag{3.5}$$

where we took the effective degrees of freedom g_* and g_s approximately equal. The factor γ gives the fraction of the horizon mass M_H that collapses to form PBHs. Its value depends on the details of the gravitational collapse and an analytical estimation [4] gives $\gamma = 0.2$. The present ratio of the abundance of PBHs with mass M over the total dark matter (DM) abundance, $f_{\mathrm{PBH}}(M) \equiv \Omega_{\mathrm{PBH}}(M)/\Omega_{\mathrm{DM}}$, can be expressed as

$$f_{\mathrm{PBH}}(M) \equiv \frac{\Omega_{\mathrm{PBH}}}{\Omega_{\mathrm{DM}}} = \left(\frac{\beta(M)}{3.3\times 10^{-14}}\right)\left(\frac{\Omega_{\mathrm{DM}}h^2}{0.12}\right)^{-1} \times \left(\frac{\gamma}{0.2}\right)^{\frac{3}{2}}\left(\frac{g_*}{106.75}\right)^{-\frac{1}{4}}\left(\frac{M}{10^{-12}\,M_\odot}\right)^{-1/2}. \tag{3.6}$$

The abundance of PBHs produced during RD can be significant if the scalar spectrum is amplified by roughly 7 orders of magnitude. In our single field models, described by the α-attractors potential (3.2), such an enhancement is achieved if the potential involves several steps or a step and an inflection point. In Fig. 12 we plot the PBH fractional abundance for a potential with a step and inflection point, for the parameter values listed in Sec. III A. The scalar power spectrum of this model is depicted in Fig. 14. For the estimation of the PBH abundance we assumed a threshold value $\delta_c = 0.45$ [124]. We see that, although the scalar power spectrum is characterized by an oscillatory pattern around the peak of the PBH abundance, it is predominantly monochromatic. However, the induced GW spectrum is much more informative, as we will discuss in the following.

2. Matter-dominated era

PBHs might also form in the matter-dominated era (MD). In the absence of pressure, even minute perturbations will evolve and deviations from spherical configurations play an essential role. References [129–131] examined the PBH production in a matter-dominated universe and considered the nonspherical effects during gravitational collapse. The PBH production rate β tends to be proportional to the fifth power of the variance σ [131]:

$$\beta(\sigma) = 0.056\sigma^5. \tag{3.7}$$

This expression has been derived with semianalytical calculations and applies to $0.005 \lesssim \sigma \lesssim 0.2$, whereas for $\sigma \lesssim 0.005$ the PBH production rate is modified if there is significant angular momentum in the collapsing region [132]. The PBH fractional abundance is

$$f_{\mathrm{PBH}} \simeq 1.3\times 10^9 \gamma\beta \frac{T_{\mathrm{rh}}}{\mathrm{GeV}}, \tag{3.8}$$

with T_{rh} is the reheating temperature.

There are two very interesting implications of PBH production during the MD era. First, the PBH abundance is found to be larger compared to RD for a given amplitude of

the curvature power spectrum. Inflationary potentials with steps, which enhance the curvature power spectrum by 4 or 5 orders of magnitude, can have an observational effect by generating a significant cosmological PBH abundance. Second, the PBH production during the MD era yields a PBH mass spectrum that is not predominantly monochromatic. It has a distribution over a few orders of the PBH mass values, which might reveal a nontrivial shape for the underlying power spectrum of the primordial density perturbations. Although the specific inflationary models that we examine here do not have a very strong effect on the PBH mass spectrum, inflationary models with steps can in principle produce mild modulations in the distribution of PBHs. The blue curve in Fig. 12 depicts the PBH abundance produced by an inflationary potential given by Eq. (3.2) with three steps, for amplitude $\Delta_R^2 \sim 10^{-4}$ and $T_{\rm rh} \sim 10^3$ GeV. In the same figure, the dashed curve depicts the PBH abundance produced by the double-pulse model of Fig. 8 for $\Delta_R^2 \sim 10^{-3}$ and $T_{\rm rh} \sim 1$ GeV. The spectrum is sufficiently wide and oscillating in order to have an observational impact on the PBH mass distribution.

C. Induced gravitational waves

Primordial density perturbations that seed PBHs also produce stochastic GWs through the mode-mode coupling of the density perturbations beyond the linear order in the perturbative expansion. The GW production takes place mainly at the time when the perturbations reenter the Hubble horizon. If density perturbations enter during the RD era, the stochastic spectrum of second order GWs can be computed following cosmological perturbation theory [9–18]. The same density perturbations will also produce PBHs with abundance proportional to β given by Eq. (3.3). On the other hand, if perturbations enter deep in an early MD era, a different analysis has to be followed in order to find the GW energy density spectrum [133,134]. The corresponding PBH abundance will now be proportional to β given by Eq. (3.7). In the following we will consider GW production only during the RD era, leaving the study of the early MD era scenario for future work. We will also assume that curvature perturbations are described by Gaussian statistics.[1]

The spectrum of the induced GWs is sourced and shaped by the curvature perturbations. In Sec. II we found that inflationary potentials with steps generate a distinct oscillatory profile for the curvature power spectrum. We expect that this profile is transmitted to GWs. In the following subsections we will further elaborate on the modulations of the amplitude in the GW energy density spectrum, which will be found to display a multiple peak structure. We will show in particular that the amplitude and the frequency of the peaks in the GW spectrum are determined by the position and the number of the steps in the inflaton potential. The GW spectrum inherits the pattern characteristics of the curvature power spectrum and, hence, serves as a portal to the inflationary dynamics.

Different GW experiments are sensitive to different frequency bands. Curvature power spectra with a prominent peak at the horizon mass range 10^{-15}–10^{-10} $M_\odot$ generate induced GWs at the frequency band 1–10^{-4} Hz, and can be tested by space-based interferometers like LISA [100], scheduled to operate in the following decade.

1. The formalism of induced GWs

GWs are described by the tensor perturbation h_{ij} in the FRW spacetime

$$ds^2 = a^2(\tau)\left[-(1+2\phi)d\tau^2 + \left((1-2\psi)\delta_{ij} + \frac{1}{2}h_{ij}\right)dx^i dx^j\right], \tag{3.9}$$

where ϕ and ψ are scalar perturbations and vector perturbations are neglected. In the absence of anisotropic stress, which is a good approximation for our purposes, we have $\phi = \psi$. The Fourier components of the tensor modes are

$$h_{ij}(\tau, \mathbf{x}) = \sum_\lambda \int \frac{d^3k}{(2\pi)^{3/2}} h_\lambda(\tau, \mathbf{k}) e_{ij}^{(\lambda)}(\mathbf{k}) e^{i\mathbf{kx}}, \tag{3.10}$$

where $e_{ij}^{(\lambda)}$, with $\lambda = +, \times$, are polarization tensors. Through the definition of the dimensionless power spectrum

$$\langle h_\lambda(\tau, \mathbf{k}) h_\lambda(\tau, \mathbf{k}')\rangle = \delta_{\lambda\lambda'}\delta^3(\mathbf{k}+\mathbf{k}')\frac{2\pi^2}{k^3}\mathcal{P}_h(\tau, k) \tag{3.11}$$

we have

$$\rho_{\rm GW}(\tau, k) = \frac{M_{\rm Pl}^2}{8}\frac{k^2}{a^2}\overline{\mathcal{P}_h(\tau, k)}. \tag{3.12}$$

The evolution of h_{ij} is obtained by expanding the Einstein equations. At second order in scalar perturbations, the equation of motion for the Fourier components of the tensor perturbations is

$$h_\lambda'' + 2\mathcal{H}h_\lambda' + k^2 h_\lambda = 4S_\lambda(\tau, \mathbf{k}), \tag{3.13}$$

where $S_\lambda(\tau, \mathbf{k})$ is a source that consists of products of scalar perturbations:

[1]Non-Gaussian statistics may also generate modulations in the GW energy density spectrum [135].

$$S_\lambda(\tau,\mathbf{k}) = \int \frac{d^3k}{(2\pi)^{3/2}} e^{ij}(\mathbf{k}) q_i q_j \Big(2\phi_{\mathbf{q}}\phi_{\mathbf{k}-\mathbf{q}} + \frac{4}{3(1+w)} (\mathcal{H}^{-1}\phi_{\mathbf{q}} + \phi_{\mathbf{q}})(\mathcal{H}^{-1}\phi_{\mathbf{k}-\mathbf{q}} + \phi_{\mathbf{k}-\mathbf{q}}) \Big). \tag{3.14}$$

The evolution of $\phi_{\mathbf{k}}$ is given in terms of the scalar transfer function. For radiation domination, we have $\phi_{\mathbf{k}}(\tau) = \phi(x)\Phi_{\mathbf{k}}$, with

$$\phi(x) = \frac{9}{x^2}\left(\frac{\sin(x/\sqrt{3})}{x/\sqrt{3}} - \cos(x/\sqrt{3}) \right), \tag{3.15}$$

where $x = k\tau$, and $\Phi_{\mathbf{k}}$ is the primordial value, related to the curvature perturbation as

$$\langle \Phi_{\mathbf{k}} \Phi_{\mathbf{k}'} \rangle = \delta^3(\mathbf{k}+\mathbf{k}') \frac{2\pi^2}{k^3} \left(\frac{3+3w}{5+3w} \right)^2 \Delta_R^2(\tau,k). \tag{3.16}$$

The solution of Eq. (3.13) reads

$$h_\lambda(\tau,\mathbf{k}) = \frac{1}{a(\tau)} \int_0^\tau G_k(\tau,\bar{\tau}) a(\bar{\tau}) S_\lambda(\bar{\tau},\mathbf{k}) d\bar{\tau}, \tag{3.17}$$

where $G_k(\tau,\bar{\tau})$ is the Green function for Eq. (3.13). The power spectrum of induced GWs is expressed in a compact form as a double integral involving the power spectrum of the curvature perturbations [136],

$$\overline{\mathcal{P}_h(\tau,k)} = \int_0^\infty dt \int_{-1}^1 ds \mathcal{T}(s,t,\tau,k) \Delta_R^2\left(\frac{t+s+1}{2} k \right) \times \Delta_R^2\left(\frac{t-s+1}{2} k \right). \tag{3.18}$$

The overline denotes the oscillation average. The t and s variables are defined as $t = u + v - 1$, $s = u - v$, where $v = q/k$, $u = |\mathbf{k}-\mathbf{q}|/k$. The integral kernel $\mathcal{T}$ is given by the expression

$$\lim_{x\to\infty} x^2 \mathcal{T}(s,t,x) = 2\left(\frac{t(2+t)(s^2-1)}{(1-s+t)(1+s+t)} \right)^2 \frac{288(-5+s^2+t(2+t))^2}{(1-s+t)^6(1+s+t)^6} \times \left\{ \frac{\pi^2}{4}(-5+s^2+t(2+t))^2 \Theta(t-(\sqrt{3}-1) + \left(-(t-s+1)(t+s+1) + \frac{1}{2}(-5+s^2+t(2+t)) \log\left| \frac{-2+t(2+t)}{3-s^2} \right| \right)^2 \right\}, \tag{3.19}$$

where Θ is the Heaviside step function. The fraction of the GW energy density per logarithmic wave number interval is

$$\Omega_{\rm GW}(\tau,k) = \frac{1}{\rho_{\rm tot}(\tau)} \frac{d\rho_{\rm GW}(\tau,k)}{d\ln k} = \frac{1}{24}\left(\frac{k}{a(\tau)H(\tau)} \right)^2 \overline{\mathcal{P}_h(\tau,k)}. \tag{3.20}$$

At a certain time t_c the production of induced GWs ceases, while their propagation becomes free. In a RD background the energy density parameter $\Omega_{\rm GW}$ remains constant. Its value at the current time t_0 is given by Eq. (3.20) times the current radiation density parameter, $\Omega_{\gamma,0}h^2 = 4.2\times10^{-5}$, modulo changes in the number of the relativistic degrees of freedom g_* in the radiation fluid:

$$\Omega_{\rm GW}(t_0,f)h^2 = 0.39 \times \left(\frac{g_*}{106.75} \right)^{-1/3} \Omega_{\gamma,0}h^2 \times \Omega_{\rm GW}(t_c,f). \tag{3.21}$$

The total energy density parameter of induced GWs is obtained by integrating the GW energy density spectrum over the entire frequency interval.

D. Oscillations in the power spectrum of the induced GWs from potentials with steps

We start the discussion of the pattern of induced GWs produced in inflationary models with sharp features by looking at the spectrum characteristics of analytically calculable models, such as those depicted in Figs. 6–8. In Sec. II we performed a semianalytic calculation of the curvature power spectrum by modeling the function $f(N)$ of Eq. (2.8), which captures the dynamics of the inflaton field beyond the slow-roll regime, through a sequence of square pulses. The amplitude of the produced curvature power spectrum is enhanced by the factor $|C_m|^2$ of Eq. (2.21), while it also displays oscillatory patterns with characteristic periods $\delta k/H \sim e^N\pi$ in k-space, where N is the number of e-foldings at which the function $f(N)$ varies strongly. [See the discussion below Eq. (2.21).] Roughly the same characteristic frequency is observed in the GW spectra. In Fig. 13 the GW spectra for the three examples studied in Sec. II E are plotted. We also plot a harmonic function $\Omega_{\rm GW\,max}(2+\sin(\alpha_{\rm GW}k-\theta))/3$ that highlights the periodic change of the GW amplitude around the peak through a fit of the k-space period $\delta k_{\rm GW} \sim 2\pi/\alpha_{\rm GW}$. We find

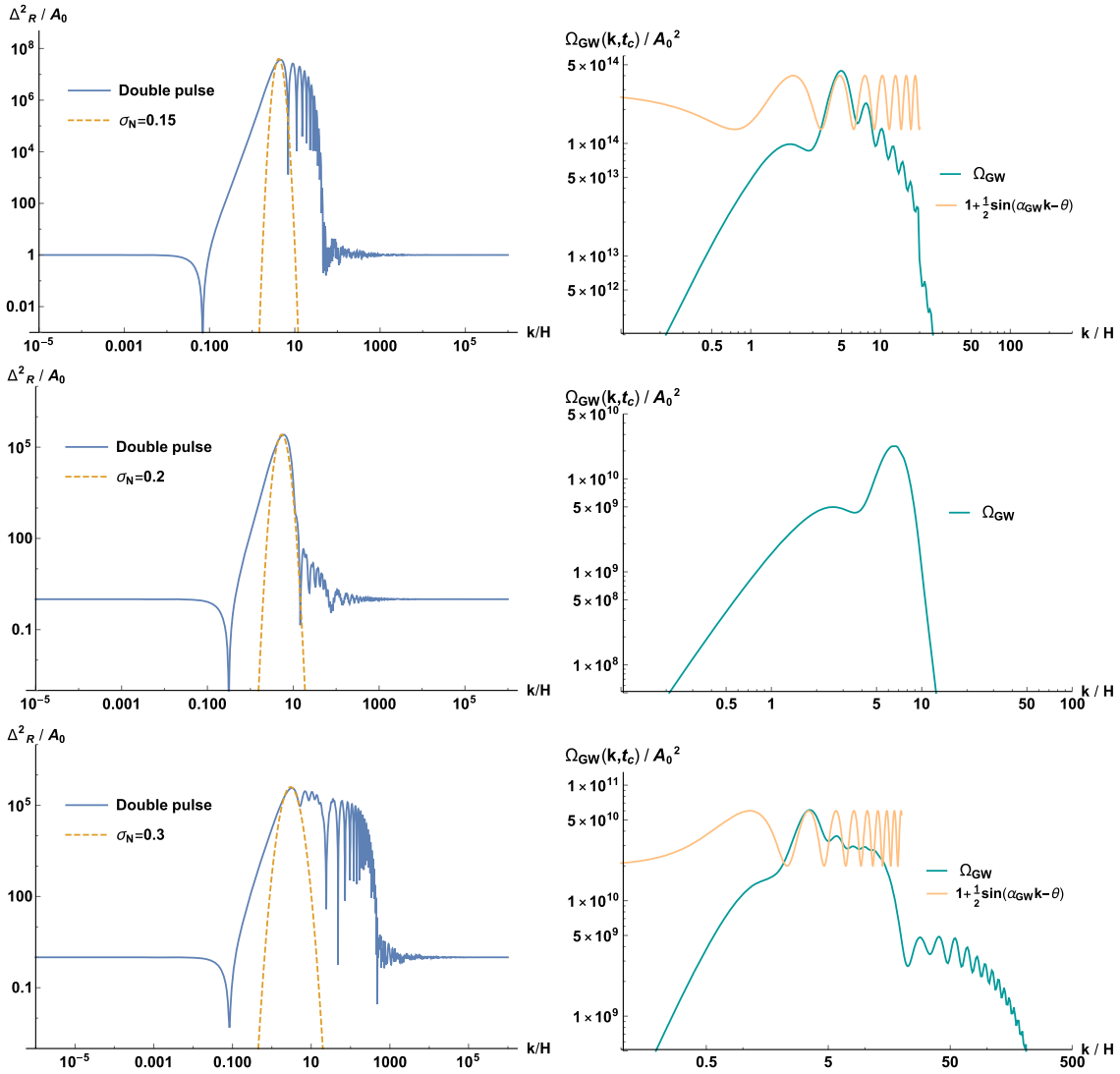

FIG. 13. Left: the scalar power spectrum produced by a double square pulse, normalized to the CMB measured amplitude. The dashed line is a log-normal power spectrum with width $\sigma_{\rm N}$. Right: the induced GW spectrum, along with a fitting harmonic function. Each row, from top to bottom, corresponds to the pulse producing the spectrum of each of Figs. 6–8, respectively.

$\alpha_{\rm GW} = \mathcal{O}(1)/H$, corresponding to the smallest period of the oscillations in the curvature spectrum $\delta k/H \sim \mathcal{O}(1)\pi$. It must be noted that larger periods of size $\delta k/H = \mathcal{O}(10)\pi$ appearing in Δ_R^2 can also be discerned in the modulations of the amplitude of the GW spectrum at the corresponding scales. However, they are less visible as they extend to regions in k-space far from the peak.

The short-period modulations of order π imply that the peaks in the curvature spectrum are narrow. In Fig. 13 a log-normal distribution with a certain width $\sigma_{\rm N} < 1$ is plotted together with Δ_R^2. It elucidates the prominent two-peak structure induced in the GW spectrum [17,95,96], which appears when the main peak of the curvature spectrum is sufficiently narrow. In our first example, for a square pulse starting at $N = 0$, corresponding to a smallest period of oscillations $\delta k/H \simeq \pi$, the peak of Δ_R^2 is found at a wave number $k_{\rm p}/H \simeq 4.5$, comparable to π. The k-range of the fitting log-normal distribution is determined by requiring that $\delta k \sim k_{\rm p}(e^{\sigma_{\rm N}} - 1)$, which implies that $\sigma_{\rm N} < 1$. As a result, and in agreement with the analysis of Ref. [95], the GW spectrum is found to feature a major, relatively sharp peak at $(2/\sqrt{3})k_{\rm p}/H$. Additionally, in the low-k side there is a relatively flat local maximum, at a wave number near $k_{\rm p}/e$. This characteristic two-peak structure is evident in all three examples we studied. In the second example in particular, in which Δ_R^2 is dominated by a single peak because the smallness of the positive pulse confines the oscillatory patterns within the high-k part of the spectrum, the two-peak structure is practically the only observable feature.

Let us now turn to the inflationary models with steplike features described by Eq. (3.2). In these models, the

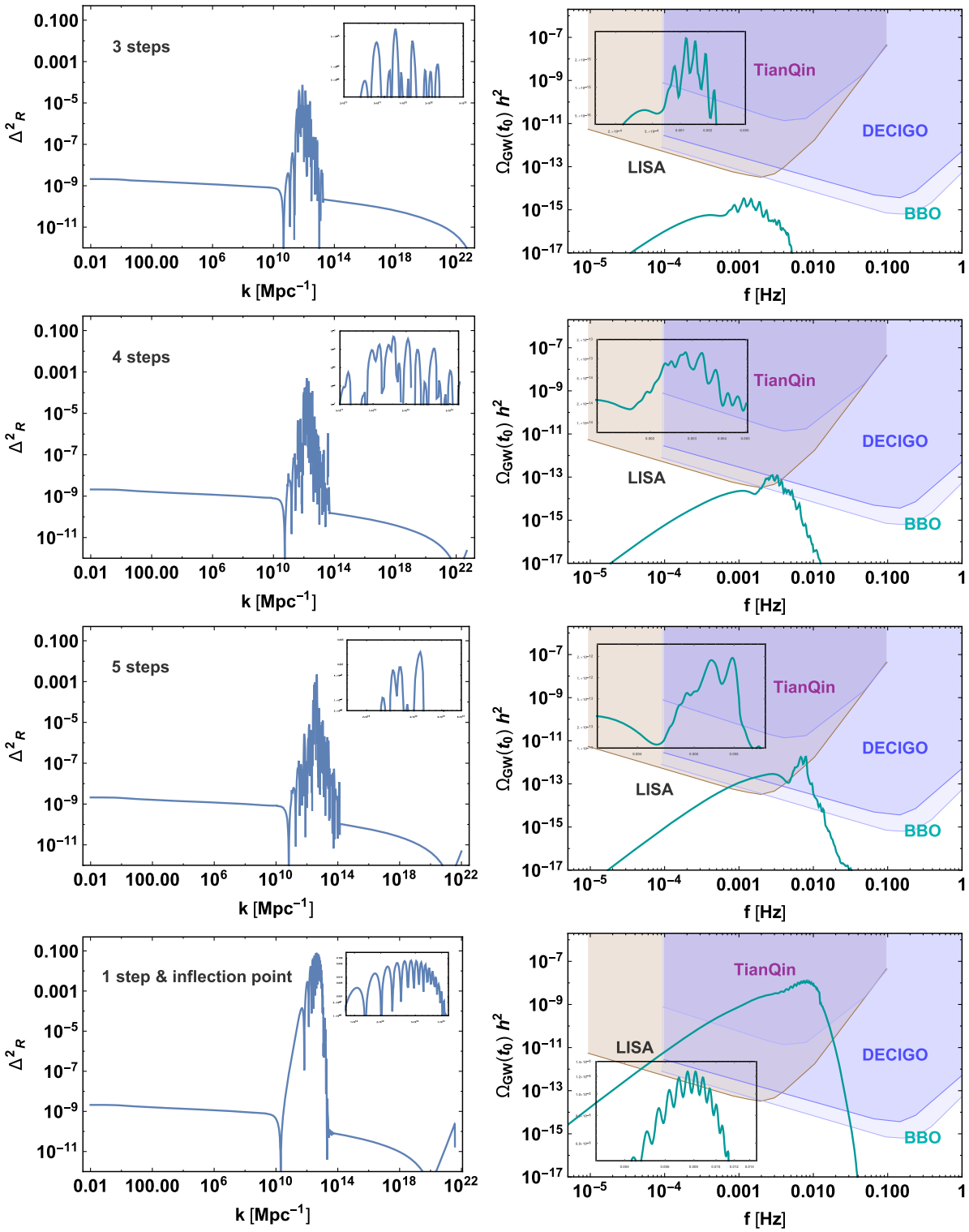

FIG. 14. Left panels: the curvature power spectra produced by inflationary models with potential given by Eq. (3.2) and depicted in Fig. 10, for parameter values given in the text. Right panels: the generated GW density parameter produced by each inflationary model. A zoom-in plot of the peak region has been included in each panel. Note that the last row of panels corresponds to an inflationary model that features both a step and an inflection point, depicted in Fig. 11.

effective-friction function $f(N)$ of Eq. (2.8), depicted in Fig. 10, has a $2n$-pulse structure for n steps, with each positive pulse followed by a negative one. In the semi-analytically calculable models that we studied before, the power spectrum was normalized such that the step features started at $N = 0$. We observed an enhancement by a factor $|C_m|^2$, together with oscillations of period $\delta k/H \sim e^N \pi$. In the inflationary models of Eq. (3.2) we find numerically similar patterns. The curvature spectrum Δ_R^2 is to a good approximation enhanced by $|C_m|^2$, with a main peak at a wave number $k_{\rm p}$ characteristic of the step position in terms of the number of e-foldings N, which are now counted from the exit of the CMB scale. Oscillations are also produced with an approximate period $\delta k \sim k_p$.

In Fig. 14 we plot four curvature power spectra together with the GW density spectra that they induce. For the three-step model, the curvature spectrum displays strong modulations and one can read off an oscillatory pattern with period $\delta k \simeq 2.5 \times 10^{11}$ Mpc^{-1}. The spectrum Δ_R^2 has three prominent peaks at comparable wave numbers $k_{\rm p1}$, $k_{\rm p2}$, $k_{\rm p3}$. Each peak is well described by a narrow log-normal distribution in the k-range with width $\sigma_{\rm N} < 1$. The combination of these three peaks induces a characteristic five-peak structure in the GW spectrum [137], along with the rather flat local maximum at lower k, as can be seen in the first row of panels in Fig. 14. The first sharp peak in the GW spectrum is located at the value $k_{\rm GW,1} = 2k_{\rm p1}/\sqrt{3}$, the second at $k_{\rm GW,2} = (k_{\rm p1} + k_{\rm p2})/\sqrt{3}$, the third at $k_{\rm GW,3} = 2k_{\rm p2}/\sqrt{3}$, the fourth at $k_{\rm GW,4} = (k_{\rm p2} + k_{\rm p3})/\sqrt{3}$ and the fifth at $k_{\rm GW,5} = 2k_{\rm p3}/\sqrt{3}$. The rather flat local maximum at lower k is located near $k_{\rm p2}/e$, where $k_{\rm p2}$ is the wave number of the highest peak. These values can be seen in Fig. 14 in the frequency spectrum and in Hz units through the conversion $f = k/(2\pi)$, where Mpc$^{-1} \simeq 0.97 \times 10^{-14}$ Hz. Similar conclusions can be drawn for the next two inflationary models that feature four and five steps, respectively.

For the inflationary model that features both an inflection point and a step, the resulting spectra are quite different compared to the previously discussed models that involve only steps. The inflection point is responsible for the strong enhancement of the curvature power spectrum and its relatively wide peak. Indeed, the envelope function that outlines the peak can be fitted by a log-normal distribution with width $\sigma_{\rm N} \simeq 0.4$. Hence the characteristic two-peak structure in the GW spectrum [95] is not very prominent here. The steplike feature has a minor contribution to the enhancement of the curvature spectrum, but it is the source of the oscillatory pattern around the peak with the characteristic period $\delta k \simeq 7 \times 10^{-11}$ Mpc^{-1}. These oscillations are also transferred to the GW spectrum. As before, the GW oscillatory pattern is well described by a harmonic function and reflects the pattern in the curvature spectrum.

It is important to emphasize that, even though it is not clearly visible in the log-plot, the oscillations near the peak are substantial: The $\Omega_{\rm GW}$ spectrum displays variations in its amplitude that are 25% of its maximal value or larger. Such modulations in the amplitude are likely to be detectable by the near-future space interferometers.

IV. CONCLUSIONS

In this paper we studied single-field inflationary models with sharp, steplike features in the potential. The evolution of the inflaton through such features leads to the violation of the slow-roll conditions, and in some cases even to the temporary interruption of inflation. The striking consequences of the transition through a generic steplike feature are the enhancement of the power spectrum of the curvature perturbations at certain scales by several orders of magnitude and the production of distinctive oscillatory patterns. We studied analytically and numerically the inflationary dynamics and we derived the expressions that describe quantitatively the size of the enhancement, as well as the profile of the oscillations. It is interesting that these features impact the power spectrum in a distinctive and predictive way that reflects their properties: the amplification and the oscillatory pattern are shaped by the position, number and steepness of the features.

Our analysis has revealed the origin of the oscillations. They are generated through the detuning of the phase difference between the real and imaginary parts of the curvature perturbation, which evolves according to the Mukahnov-Sasaki equation (2.2). When the inflaton moves through a step in the potential, the background evolution deviates strongly from the standard slow roll for a small number of e-foldings, in a way that the real and imaginary parts of the solution are detuned. The detuning results in time-dependent oscillations of the amplitude. When the perturbations asymptotically freeze at superhorizon scales, an oscillatory pattern is induced on the wave number dependence of the power spectrum. A detailed discussion of this point can be found in Ref. [79] and Secs. II B, II C, and II F. It must be emphasized that oscillations in the spectrum are not a generic consequence of any feature in the potential that violates slow roll. In contrast to a steep step, an inflection point in general induces an enhanced, but smooth, power spectrum.

From the model-building perspective, a steep step can appear if the inflationary potential includes plateaus with different energy densities. A nearly constant potential energy density can be associated with underlying symmetries that are preserved in the plateau [110]. A deformation of the symmetry results in energy splitting, so that a transition between different energy levels can be induced. Such a behavior can be captured by the framework of the inflationary models characterized as α-attractors [108,109].

A strong motivation for analyzing such models is that the induced tensor power spectrum inherits the oscillating profile of the primordial curvature spectrum. The combined pattern of an enhanced spectrum together with strong

oscillations is potentially detectable by near future space interferometers. Through the detection of the GW spectrum, one can aim at inferring at least some basic feature of the inflationary potential, such as whether steplike transitions are present. Motivated by this possibility, we examined in detail, numerically and analytically, the scalar and the induced tensor spectra and we identified correlations between them. The main characteristic property of both spectra, related to the transition through a step, is a series of peaks. Through a more refined analysis of the spectrum, one can look for more detailed information, such as the number of the steps, their position and exact shape, and whether there is, in addition to a step, an inflection point. We explored this possibility by studying several analytical examples, as well as inflationary models in the α-attractor framework, always imposing consistency with the constraints for the spectral index n_s and the amplitude of the scalar spectrum arising from the CMB measurements.

The detection of GWs from inflationary models with sharp features may be accompanied by the presence of PBHs as a significant fraction of dark matter. The enhancement of the power spectrum due to the presence of steplike features, though considerable, may be inefficient to trigger the production of a sizable number of PBHs if radiation dominates the energy density of the early Universe. However, it can be sufficient to induce gravitational collapse processes and PBH production if the universe energy density is dominated by nonrelativistic matter. We examined the profile of the PBH mass spectrum produced either in a radiation or an early matter-dominated universe, looking for deviations from the common monochromatic profile. For the latter scenario we found that this is possible because of the multiple-peak structure of the curvature power spectrum.

It is important to note that the oscillations near the peak of the GW spectrum have a scale comparable to that of its maximal value. Such modulations in the amplitude are likely to be detectable by the near future space interferometers, such as LISA. This demonstrates that induced GWs can be used as a powerful tool for probing the inflationary potential. The detection of oscillatory patterns in the amplitude of the GW spectrum will be a strong indication for sharp features in the potential of single-field inflation.

ACKNOWLEDGMENTS

We would like to thank V. Spanos for useful discussions. The work of I. Dalianis, G. Kodaxis, I. Stamou and N. Tetradis was supported by the Hellenic Foundation for Research and Innovation (H.F.R.I.) under the First Call for H.F.R.I. Research Projects to support Faculty members and Researchers and the procurement of high-cost research equipment grant (Project No. 824).

[1] Ya. B. Zeldovich and I. D. Novikov, The hypothesis of cores retarded during expansion and the hot cosmological model, Sov. Astron. **10**, 602 (1967).
[2] S. Hawking, Gravitationally collapsed objects of very low mass, Mon. Not. R. Astron. Soc. **152**, 75 (1971).
[3] B. J. Carr and S. W. Hawking, Black holes in the early Universe, Mon. Not. R. Astron. Soc. **168**, 399 (1974).
[4] B. J. Carr, The primordial black hole mass spectrum, Astrophys. J. **201**, 1 (1975).
[5] B. Carr, F. Kuhnel, and M. Sandstad, Primordial black holes as dark matter, Phys. Rev. D **94**, 083504 (2016).
[6] M. Sasaki, T. Suyama, T. Tanaka, and S. Yokoyama, Primordial black holes—Perspectives in gravitational wave astronomy, Classical Quantum Gravity **35**, 063001 (2018).
[7] B. Carr and F. Kuhnel, Primordial black holes as dark matter: Recent developments, Annu. Rev. Nucl. Part. Sci. **70**, 355 (2020).
[8] A. M. Green and B. J. Kavanagh, Primordial black holes as a dark matter candidate, J. Phys. G **48**, 043001 (2021).
[9] S. Matarrese, O. Pantano, and D. Saez, A general relativistic approach to the nonlinear evolution of collisionless matter, Phys. Rev. D **47**, 1311 (1993).
[10] S. Matarrese, O. Pantano, and D. Saez, General Relativistic Dynamics of Irrotational Dust: Cosmological Implications, Phys. Rev. Lett. **72**, 320 (1994).
[11] S. Matarrese, S. Mollerach, and M. Bruni, Second order perturbations of the Einstein–de Sitter universe, Phys. Rev. D **58**, 043504 (1998).
[12] S. Mollerach, D. Harari, and S. Matarrese, CMB polarization from secondary vector and tensor modes, Phys. Rev. D **69**, 063002 (2004).
[13] H. Noh and J. c. Hwang, Second-order perturbations of the Friedmann world model, Phys. Rev. D **69**, 104011 (2004).
[14] C. Carbone and S. Matarrese, A unified treatment of cosmological perturbations from super-horizon to small scales, Phys. Rev. D **71**, 043508 (2005).
[15] K. Nakamura, Second-order gauge invariant cosmological perturbation theory: Einstein equations in terms of gauge invariant variables, Prog. Theor. Phys. **117**, 17 (2007).
[16] D. Baumann, P. J. Steinhardt, K. Takahashi, and K. Ichiki, Gravitational wave spectrum induced by primordial scalar perturbations, Phys. Rev. D **76**, 084019 (2007).
[17] K. N. Ananda, C. Clarkson, and D. Wands, The cosmological gravitational wave background from primordial density perturbations, Phys. Rev. D **75**, 123518 (2007).
[18] H. Assadullahi and D. Wands, Gravitational waves from an early matter era, Phys. Rev. D **79**, 083511 (2009).

[19] N. Aghanim *et al.* (Planck Collaboration), Planck 2018 results. VI. Cosmological parameters, Astron. Astrophys. **641**, A6 (2020).
[20] P. Ivanov, P. Naselsky, and I. Novikov, Inflation and primordial black holes as dark matter, Phys. Rev. D **50**, 7173 (1994).
[21] J. Yokoyama, Chaotic new inflation and formation of primordial black holes, Phys. Rev. D **58**, 083510 (1998).
[22] S. L. Cheng, W. Lee, and K. W. Ng, Production of high stellar-mass primordial black holes in trapped inflation, J. High Energy Phys. 02 (2017) 008.
[23] J. Garcia-Bellido and E. Ruiz Morales, Primordial black holes from single field models of inflation, Phys. Dark Universe **18**, 47 (2017).
[24] J. M. Ezquiaga, J. Garcia-Bellido, and E. Ruiz Morales, Primordial black hole production in critical Higgs inflation, Phys. Lett. B **776**, 345 (2018).
[25] C. Germani and T. Prokopec, On primordial black holes from an inflection point, Phys. Dark Universe **18**, 6 (2017).
[26] H. Motohashi and W. Hu, Primordial black holes and slow-roll violation, Phys. Rev. D **96**, 063503 (2017).
[27] S. L. Cheng, W. Lee, and K. W. Ng, Primordial black holes and associated gravitational waves in axion monodromy inflation, J. Cosmol. Astropart. Phys. 07 (2018) 001.
[28] H. Di and Y. Gong, Primordial black holes and second order gravitational waves from ultra-slow-roll inflation, J. Cosmol. Astropart. Phys. 07 (2018) 007.
[29] G. Ballesteros and M. Taoso, Primordial black hole dark matter from single field inflation, Phys. Rev. D **97**, 023501 (2018).
[30] M. P. Hertzberg and M. Yamada, Primordial black holes from polynomial potentials in single field inflation, Phys. Rev. D **97**, 083509 (2018).
[31] O. Özsoy, S. Parameswaran, G. Tasinato, and I. Zavala, Mechanisms for primordial black hole production in string theory, J. Cosmol. Astropart. Phys. 07 (2018) 005.
[32] M. Cicoli, V. A. Diaz, and F. G. Pedro, Primordial black holes from string inflation, J. Cosmol. Astropart. Phys. 06 (2018) 034.
[33] M. Biagetti, G. Franciolini, A. Kehagias, and A. Riotto, Primordial black holes from inflation and quantum diffusion, J. Cosmol. Astropart. Phys. 07 (2018) 032.
[34] I. Dalianis, A. Kehagias, and G. Tringas, Primordial black holes from α-attractors, J. Cosmol. Astropart. Phys. 01 (2019) 037.
[35] T. J. Gao and Z. K. Guo, Primordial black hole production in inflationary models of supergravity with a single chiral superfield, Phys. Rev. D **98**, 063526 (2018).
[36] Y. Tada and S. Yokoyama, Primordial black hole tower: Dark matter, earth-mass, and LIGO black holes, Phys. Rev. D **100**, 023537 (2019).
[37] I. Dalianis and G. Tringas, Primordial black hole remnants as dark matter produced in thermal, matter, and runaway-quintessence postinflationary scenarios, Phys. Rev. D **100**, 083512 (2019).
[38] V. Atal, J. Cid, A. Escrivà, and J. Garriga, PBH in single field inflation: The effect of shape dispersion and non-Gaussianities, J. Cosmol. Astropart. Phys. 05 (2020) 022.
[39] R. Mahbub, Primordial black hole formation in inflationary α-attractor models, Phys. Rev. D **101**, 023533 (2020).
[40] S. S. Mishra and V. Sahni, Primordial black holes from a tiny bump/dip in the Inflaton potential, J. Cosmol. Astropart. Phys. 04 (2020) 007.
[41] G. Ballesteros, J. Rey, and F. Rompineve, Detuning primordial black hole dark matter with early matter domination and axion monodromy, J. Cosmol. Astropart. Phys. 06 (2020) 014.
[42] D. V. Nanopoulos, V. C. Spanos, and I. D. Stamou, Primordial black holes from no-scale supergravity, Phys. Rev. D **102**, 083536 (2020).
[43] I. D. Stamou, Mechanisms of producing primordial black holes by breaking the $SU(2,1)/SU(2) \times U(1)$ symmetry, Phys. Rev. D **103**, 083512 (2021).
[44] J. Liu, Z. K. Guo, and R. G. Cai, Analytical approximation of the scalar spectrum in the ultraslow-roll inflationary models, Phys. Rev. D **101**, 083535 (2020).
[45] J. Garcia-Bellido, A. D. Linde, and D. Wands, Density perturbations and black hole formation in hybrid inflation, Phys. Rev. D **54**, 6040 (1996).
[46] M. Kawasaki, N. Sugiyama, and T. Yanagida, Primordial black hole formation in a double inflation model in supergravity, Phys. Rev. D **57**, 6050 (1998).
[47] P. H. Frampton, M. Kawasaki, F. Takahashi, and T. T. Yanagida, Primordial black holes as all dark matter, J. Cosmol. Astropart. Phys. 04 (2010) 023.
[48] S. Clesse and J. García-Bellido, Massive primordial black holes from hybrid inflation as dark matter and the seeds of galaxies, Phys. Rev. D **92**, 023524 (2015).
[49] M. Kawasaki, A. Kusenko, Y. Tada, and T. T. Yanagida, Primordial black holes as dark matter in supergravity inflation models, Phys. Rev. D **94**, 083523 (2016).
[50] K. Inomata, M. Kawasaki, K. Mukaida, Y. Tada, and T. T. Yanagida, Inflationary primordial black holes as all dark matter, Phys. Rev. D **96**, 043504 (2017).
[51] J. R. Espinosa, D. Racco, and A. Riotto, Cosmological Signature of the Standard Model Higgs Vacuum Instability: Primordial Black Holes as Dark Matter, Phys. Rev. Lett. **120**, 121301 (2018).
[52] K. Inomata, M. Kawasaki, K. Mukaida, and T. T. Yanagida, Double inflation as a single origin of primordial black holes for all dark matter and LIGO observations, Phys. Rev. D **97**, 043514 (2018).
[53] M. Kawasaki, H. Nakatsuka, and I. Obata, Generation of primordial black holes and gravitational waves from dilaton-gauge field dynamics, J. Cosmol. Astropart. Phys. 05 (2020) 007.
[54] G. A. Palma, S. Sypsas, and C. Zenteno, Seeding Primordial Black Holes in Multifield Inflation, Phys. Rev. Lett. **125**, 121301 (2020).
[55] J. Fumagalli, S. Renaux-Petel, J. W. Ronayne, and L. T. Witkowski, Turning in the landscape: A new mechanism for generating primordial black holes, arXiv:2004.08369.
[56] M. Braglia, D. K. Hazra, F. Finelli, G. F. Smoot, L. Sriramkumar, and A. A. Starobinsky, Generating PBHs and small-scale GWs in two-field models of inflation, J. Cosmol. Astropart. Phys. 08 (2020) 001.

[57] Y. Aldabergenov, A. Addazi, and S. V. Ketov, Primordial black holes from modified supergravity, Eur. Phys. J. C **80**, 917 (2020).

[58] K. Kannike, L. Marzola, M. Raidal, and H. Veermäe, Single field double inflation and primordial black holes, J. Cosmol. Astropart. Phys. 09 (2017) 020.

[59] S. Pi, Y. l. Zhang, Q. G. Huang, and M. Sasaki, Scalaron from R^2-gravity as a heavy field, J. Cosmol. Astropart. Phys. 05 (2018) 042.

[60] C. Fu, P. Wu, and H. Yu, Primordial black holes from inflation with nonminimal derivative coupling, Phys. Rev. D **100**, 063532 (2019).

[61] I. Dalianis, S. Karydas, and E. Papantonopoulos, Generalized non-minimal derivative coupling: Application to inflation and primordial black hole production, J. Cosmol. Astropart. Phys. 06 (2020) 040.

[62] D. Y. Cheong, S. M. Lee, and S. C. Park, Primordial black holes in Higgs-R^2 inflation as the whole of dark matter, J. Cosmol. Astropart. Phys. 01 (2021) 032.

[63] J. Lin, Q. Gao, Y. Gong, Y. Lu, C. Zhang, and F. Zhang, Primordial black holes and secondary gravitational waves from k and G inflation, Phys. Rev. D **101**, 103515 (2020).

[64] M. Kawasaki, N. Kitajima, and T. T. Yanagida, Primordial black hole formation from an axionlike curvaton model, Phys. Rev. D **87**, 063519 (2013).

[65] K. Kohri, C. M. Lin, and T. Matsuda, Primordial black holes from the inflating curvaton, Phys. Rev. D **87**, 103527 (2013).

[66] K. Ando, K. Inomata, M. Kawasaki, K. Mukaida, and T. T. Yanagida, Primordial black holes for the LIGO events in the axionlike curvaton model, Phys. Rev. D **97**, 123512 (2018).

[67] K. Ando, M. Kawasaki, and H. Nakatsuka, Formation of primordial black holes in an axionlike curvaton model, Phys. Rev. D **98**, 083508 (2018).

[68] R. G. Cai, Z. K. Guo, J. Liu, L. Liu, and X. Y. Yang, Primordial black holes and gravitational waves from parametric amplification of curvature perturbations, J. Cosmol. Astropart. Phys. 06 (2020) 013.

[69] Y. F. Cai, X. Tong, D. G. Wang, and S. F. Yan, Primordial Black Holes from Sound Speed Resonance during Inflation, Phys. Rev. Lett. **121**, 081306 (2018).

[70] Y. F. Cai, C. Chen, X. Tong, D. G. Wang, and S. F. Yan, When primordial black holes from sound speed resonance meet a stochastic background of gravitational waves, Phys. Rev. D **100**, 043518 (2019).

[71] C. Chen and Y. F. Cai, Primordial black holes from sound speed resonance in the inflaton-curvaton mixed scenario, J. Cosmol. Astropart. Phys. 10 (2019) 068.

[72] C. Chen, X. H. Ma, and Y. F. Cai, Dirac-Born-Infeld realization of sound speed resonance mechanism for primordial black holes, Phys. Rev. D **102**, 063526 (2020).

[73] Z. Zhou, J. Jiang, Y. F. Cai, M. Sasaki, and S. Pi, Primordial black holes and gravitational waves from resonant amplification during inflation, Phys. Rev. D **102**, 103527 (2020).

[74] A. A. Starobinsky, Spectrum of adiabatic perturbations in the Universe when there are singularities in the inflation potential, JETP Lett. **55**, 489 (1992).

[75] J. A. Adams, B. Cresswell, and R. Easther, Inflationary perturbations from a potential with a step, Phys. Rev. D **64**, 123514 (2001).

[76] S. M. Leach and A. R. Liddle, Inflationary perturbations near horizon crossing, Phys. Rev. D **63**, 043508 (2001).

[77] S. M. Leach, M. Sasaki, D. Wands, and A. R. Liddle, Enhancement of superhorizon scale inflationary curvature perturbations, Phys. Rev. D **64**, 023512 (2001).

[78] D. K. Hazra, M. Aich, R. K. Jain, L. Sriramkumar, and T. Souradeep, Primordial features due to a step in the inflaton potential, J. Cosmol. Astropart. Phys. 10 (2010) 008.

[79] K. Kefala, G. P. Kodaxis, I. D. Stamou, and N. Tetradis, Features of the inflaton potential and the power spectrum of cosmological perturbations, Phys. Rev. D **104**, 023506 (2021).

[80] G. Ballesteros, J. Beltran Jimenez, and M. Pieroni, Black hole formation from a general quadratic action for inflationary primordial fluctuations, J. Cosmol. Astropart. Phys. 06 (2019) 016.

[81] J. Fumagalli, S. Renaux-Petel, and L. T. Witkowski, Oscillations in the stochastic gravitational wave background from sharp features and particle production during inflation, J. Cosmol. Astropart. Phys. 08 (2021) 030.

[82] M. Braglia, X. Chen, and D. K. Hazra, Probing primordial features with the stochastic gravitational wave background, J. Cosmol. Astropart. Phys. 03 (2021) 005.

[83] J. Fumagalli, S. é. Renaux-Petel, and L. T. Witkowski, Resonant features in the stochastic gravitational wave background, J. Cosmol. Astropart. Phys. 08 (2021) 059.

[84] J. A. Adams, G. G. Ross, and S. Sarkar, Multiple inflation, Nucl. Phys. **B503**, 405 (1997).

[85] L. Covi, J. Hamann, A. Melchiorri, A. Slosar, and I. Sorbera, Inflation and WMAP three year data: Features have a future!, Phys. Rev. D **74**, 083509 (2006).

[86] J. Hamann, L. Covi, A. Melchiorri, and A. Slosar, New constraints on oscillations in the primordial spectrum of inflationary perturbations, Phys. Rev. D **76**, 023503 (2007).

[87] Z. G. Liu, J. Zhang, and Y. S. Piao, Phantom inflation with a steplike potential, Phys. Lett. B **697**, 407 (2011).

[88] A. Gallego Cadavid, A. E. Romano, and S. Gariazzo, Effects of local features of the inflaton potential on the spectrum and bispectrum of primordial perturbations, Eur. Phys. J. C **76**, 385 (2016).

[89] A. Gallego Cadavid, A. E. Romano, and S. Gariazzo, CMB anomalies and the effects of local features of the inflaton potential, Eur. Phys. J. C **77**, 242 (2017).

[90] M. A. Fard and S. Baghram, Late time sky as a probe of steps and oscillations in primordial Universe, J. Cosmol. Astropart. Phys. 01 (2018) 051.

[91] N. Kaloper and M. Kaplinghat, Primeval corrections to the CMB anisotropies, Phys. Rev. D **68**, 123522 (2003).

[92] G. D'Amico and N. Kaloper, Rollercoaster cosmology, J. Cosmol. Astropart. Phys. 08 (2021) 058.

[93] G. D'Amico, N. Kaloper, and A. Westphal, Double monodromy inflation: A gravity waves factory for CMB-S4, LiteBIRD and LISA, Phys. Rev. D **104**, 081302 (2021).

[94] R. G. Cai, S. Pi, and M. Sasaki, Universal infrared scaling of gravitational wave background spectra, Phys. Rev. D **102**, 083528 (2020).
[95] S. Pi and M. Sasaki, Gravitational waves induced by scalar perturbations with a log-normal peak, J. Cosmol. Astropart. Phys. 09 (2020) 037.
[96] R. Saito and J. Yokoyama, Gravitational Wave Background as a Probe of the Primordial Black Hole Abundance, Phys. Rev. Lett. **102**, 161101 (2009); **107**, 069901 (E) (2011).
[97] I. Dalianis and K. Kritos, Exploring the spectral shape of gravitational waves induced by primordial scalar perturbations and connection with the primordial black hole scenarios, Phys. Rev. D **103**, 023505 (2021).
[98] B. P. Abbott *et al.* (LIGO Scientific and Virgo Collaborations), Upper Limits on the Stochastic Gravitational-Wave Background from Advanced LIGO's First Observing Run, Phys. Rev. Lett. **118**, 121101 (2017); Erratum, Phys. Rev. Lett. **119**, 029901 (2017).
[99] Z. C. Chen, C. Yuan, and Q. G. Huang, Pulsar Timing Array Constraints on Primordial Black Holes with NANOGrav 11-Year Dataset, Phys. Rev. Lett. **124**, 251101 (2020).
[100] P. Amaro-Seoane *et al.* (LISA Collaboration), Laser interferometer space antenna, arXiv:1702.00786.
[101] W. H. Ruan, Z. K. Guo, R. G. Cai, and Y. Z. Zhang, Taiji program: Gravitational-wave sources, Int. J. Mod. Phys. A **35**, 2050075 (2020).
[102] J. Luo *et al.* (TianQin Collaboration), TianQin: A space-borne gravitational wave detector, Classical Quantum Gravity **33**, 035010 (2016).
[103] N. Seto, S. Kawamura, and T. Nakamura, Possibility of Direct Measurement of the Acceleration of the Universe using 0.1-Hz Band Laser Interferometer Gravitational Wave Antenna in Space, Phys. Rev. Lett. **87**, 221103 (2001).
[104] S. Sato, S. Kawamura, M. Ando, T. Nakamura, K. Tsubono, A. Araya, I. Funaki, K. Ioka, N. Kanda, S. Moriwaki *et al.*, The status of DECIGO, J. Phys. Conf. Ser. **840**, 012010 (2017).
[105] B. Sathyaprakash, M. Abernathy, F. Acernese, P. Ajith, B. Allen, P. Amaro-Seoane, N. Andersson, S. Aoudia, K. Arun, P. Astone *et al.*, Scientific objectives of Einstein telescope, Classical Quantum Gravity **29**, 124013 (2012); Erratum, Classical Quantum Gravity **30**, 079501 (2013).
[106] C. Wetterich, Exact evolution equation for the effective potential, Phys. Lett. B **301**, 90 (1993).
[107] J. Berges, N. Tetradis, and C. Wetterich, Nonperturbative renormalization flow in quantum field theory and statistical physics, Phys. Rep. **363**, 223 (2002).
[108] R. Kallosh and A. Linde, Universality class in conformal inflation, J. Cosmol. Astropart. Phys. 07 (2013) 002.
[109] S. Ferrara, R. Kallosh, A. Linde, and M. Porrati, Minimal supergravity models of inflation, Phys. Rev. D **88**, 085038 (2013).
[110] R. Kallosh, A. Linde, and D. Roest, Large field inflation and double α-attractors, J. High Energy Phys. 08 (2014) 052.
[111] A. A. Starobinsky, A new type of isotropic cosmological models without singularity, Phys. Lett. **91B**, 99 (1980).
[112] V. F. Mukhanov, H. Feldman, and R. H. Brandenberger, Theory of cosmological perturbations. Part 1. Classical perturbations. Part 2. Quantum theory of perturbations. Part 3. Extensions, Phys. Rep. **215**, 203 (1992).
[113] V. F. Mukhanov, Quantum theory of gauge invariant cosmological perturbations, Sov. Phys. JETP **67**, 1297 (1988).
[114] M. Sasaki, Large scale quantum fluctuations in the inflationary Universe, Prog. Theor. Phys. **76**, 1036 (1986).
[115] C. T. Byrnes, P. S. Cole, and S. P. Patil, Steepest growth of the power spectrum and primordial black holes, J. Cosmol. Astropart. Phys. 06 (2019) 028.
[116] P. Carrilho, K. A. Malik, and D. J. Mulryne, Dissecting the growth of the power spectrum for primordial black holes, Phys. Rev. D **100**, 103529 (2019).
[117] O. Özsoy and G. Tasinato, On the slope of the curvature power spectrum in non-attractor inflation, J. Cosmol. Astropart. Phys. 04 (2020) 048.
[118] Y. Akrami *et al.* (Planck Collaboration), Planck 2018 results. X. Constraints on inflation, Astron. Astrophys. **641**, A10 (2020).
[119] B. Carr, K. Kohri, Y. Sendouda, and J. Yokoyama, Constraints on primordial black holes, arXiv:2002.12778.
[120] W. H. Press and P. Schechter, Formation of galaxies and clusters of galaxies by self-similar gravitational condensation, Astrophys. J. **187**, 425 (1974).
[121] J. C. Niemeyer and K. Jedamzik, Near-Critical Gravitational Collapse and the Initial Mass Function of Primordial Black Holes, Phys. Rev. Lett. **80**, 5481 (1998).
[122] M. Shibata and M. Sasaki, Black hole formation in the Friedmann universe: Formulation and computation in numerical relativity, Phys. Rev. D **60**, 084002 (1999).
[123] I. Musco, J. C. Miller, and A. G. Polnarev, Primordial black hole formation in the radiative era: Investigation of the critical nature of the collapse, Classical Quantum Gravity **26**, 235001 (2009).
[124] I. Musco and J. C. Miller, Primordial black hole formation in the early Universe: Critical behavior and self-similarity, Classical Quantum Gravity **30**, 145009 (2013).
[125] T. Harada, C. M. Yoo, and K. Kohri, Threshold of primordial black hole formation, Phys. Rev. D **88**, 084051 (2013); **89**, 029903(E) (2014).
[126] C. Germani and I. Musco, The Abundance of Primordial Black Holes Depends on the Shape of the Inflationary Power Spectrum, Phys. Rev. Lett. **122**, 141302 (2019).
[127] C. T. Byrnes, M. Hindmarsh, S. Young, and M. R. S. Hawkins, Primordial black holes with an accurate QCD equation of state, J. Cosmol. Astropart. Phys. 08 (2018) 041.
[128] S. Young, C. T. Byrnes, and M. Sasaki, Calculating the mass fraction of primordial black holes, J. Cosmol. Astropart. Phys. 07 (2014) 045.
[129] M. Y. Khlopov and A. G. Polnarev, Primordial black holes as a cosmological test of grand unification, Phys. Lett. **97B**, 383 (1980).
[130] A. G. Polnarev and M. Y. Khlopov, Cosmology, primordial black holes, and supermassive particles, Usp.

Fiz. Nauk **145**, 369 (1985) [Sov. Phys. Usp. **28**, 213 (1985)].

[131] T. Harada, C. M. Yoo, K. Kohri, K. i. Nakao, and S. Jhingan, Primordial black hole formation in the matter-dominated phase of the Universe, Astrophys. J. **833**, 61 (2016).

[132] T. Harada, C. M. Yoo, K. Kohri, and K. I. Nakao, Spins of primordial black holes formed in the matter-dominated phase of the Universe, Phys. Rev. D **96**, 083517 (2017); Erratum, Phys. Rev. D **99**, 069904 (2019).

[133] K. Jedamzik, M. Lemoine, and J. Martin, Generation of gravitational waves during early structure formation between cosmic inflation and reheating, J. Cosmol. Astropart. Phys. 04 (2010) 021.

[134] I. Dalianis and C. Kouvaris, Gravitational waves from density perturbations in an early matter domination era, J. Cosmol. Astropart. Phys. 07 (2021) 046.

[135] R. g. Cai, S. Pi, and M. Sasaki, Gravitational Waves Induced by Non-Gaussian Scalar Perturbations, Phys. Rev. Lett. **122**, 201101 (2019).

[136] K. Kohri and T. Terada, Semianalytic calculation of gravitational wave spectrum nonlinearly induced from primordial curvature perturbations, Phys. Rev. D **97**, 123532 (2018).

[137] R. G. Cai, S. Pi, S. J. Wang, and X. Y. Yang, Resonant multiple peaks in the induced gravitational waves, J. Cosmol. Astropart. Phys. 05 (2019) 013.